JGR Planets

RESEARCH ARTICLE
10.1029/2023JE007800

Key Points:

- We created a radiative heat transfer model that simulates light scattering and absorption in granular media with irregular surfaces
- Using the model, we simulated solar warming of snow-like morphologies relevant to Europa to gain insight into penitente growth
- Results suggest that taller, sharper penitentes with coarse grains and low thermal inertia are more likely to grow at Europa's equator

Correspondence to:
D. B. Goldstein,
david@oden.utexas.edu

Citation:
Carreon, A., Macias, A., Hsu, A., Berisford, D. F., Goldstein, D. B., Varghese, P., et al. (2023). Simulating radiative heat transfer in multi-scattering irregular surfaces: Application to snow and ice morphologies on Europa. *Journal of Geophysical Research: Planets*, *128*, e2023JE007800. https://doi.org/10.1029/2023JE007800

Received 9 MAR 2023
Accepted 9 OCT 2023

Simulating Radiative Heat Transfer in Multi-Scattering Irregular Surfaces: Application to Snow and Ice Morphologies on Europa

Anthony Carreon[1,2], Antonio Macias[1,2], Andy Hsu[1,2], Daniel F. Berisford[2,3], David B. Goldstein[1], Philip Varghese[1], Laurence Trafton[1], Kevin P. Hand[2], Jordan Steckloff[1], and Arnaud Mahieux[1]

[1]The University of Texas at Austin, Austin, TX, USA, [2]Jet Propulsion Laboratory, California Institute of Technology, Pasadena, CA, USA, [3]Airborne Snow Observatories, Inc., Mammoth Lakes, CA, USA

Abstract We developed a Monte-Carlo-based radiative heat transfer model capable of simulating solar exposure and subsequent warming of rough snow and ice surfaces on ice-covered airless solar system bodies. The model accounts for wavelength-dependent internal light scattering and heat conduction in the snow interior down to meter-scale depths. We validated the model against analytical and experimental test cases with relevant applications to Europa, one of Jupiter's moons. We examined differential heating across the surface, from the centimeter to meter scale, to reveal potential patterns of preferential sublimation that could lead to rough ice morphologies, such as penitentes. An exploration of parameters such as penitente height-width ratios, shape, size, snow grain size, and thermal properties revealed that taller, thinner, larger penitentes with sharper peaks, coarser snow grain sizes, and lower thermal inertias are more likely to grow in Europa's environment near the equator.

Plain Language Summary Penitentes are sharp, bladed snow structures found on Earth in cold, dry regions with high Sun exposure. Speculated to exist on Jupiter's moon Europa, these formations could pose a hazard for a future lander spacecraft. To determine whether such structures could be present, we developed a computer model that simulates snow warming by the Sun within Europa's cold, dry, vacuum environment. Initial results suggest that penitente growth is possible under certain geometric, optical, and thermal conditions applicable to Europa's environment near the equator.

1. Introduction

The morphological evolution of ice under varying temperatures, pressure, and Sun exposure is particularly interesting for Earth's cryosphere and icy planets and moons elsewhere in our solar system. One specific morphology that forms in sublimation-driven environments on Earth (and is proposed to exist elsewhere) are sharp, pointed, Sun-directed constructs known as penitentes, which are often found in cool regions with high Sun exposure and low humidity, such as the Andes Mountains and Mount Kilimanjaro in Africa (see Figure 1). These structures tend to align their blade-like axes with the plane of the Sun's path across the sky. Numerous authors have proposed theories on their formation (Amstutz, 1958; Betterton, 2001; Lliboitry, 1954; Troll, 1942), with perhaps the leading theory developed by Claudin et al. (2015).

Penitente formation is driven by nonuniform sublimation, in which ice sublimates faster in the valleys between penitentes than toward the peaks. A flat snow field will initially contain random depressions that refine over time. According to Claudin et al. (2015), penitente formation is described by a dispersion relation—a balance of geometric focusing of sunlight toward the valleys, light penetration into the snow, thermal conduction, and molecular diffusion of sublimated ice away from the surface through a vapor boundary layer. Under the right conditions, this relation predicts a sublimation instability with a dominant wavelength that defines the spacing and, therefore, the maximum possible size of penitentes.

Penitente formation may not be limited to Earth. Moores et al. (2017) have identified candidate penitentes on Pluto from *New Horizons* observations with growth mechanisms that are consistent with the Claudin et al. (2015) theory. Nguyen et al. (2019) show that Mars may harbor penitentes at the polar ice caps on inclined terrain. Jupiter's moon Europa has also been proposed as a site of penitente formation (Hobley et al., 2018); however, as detailed by Hand et al. (2020), penitente growth is unlikely in the hard vacuum of the Europa surface environment.

Figure 1. A field of penitentes on the Northern Ice Field atop Mount Kilimanjaro. Given the equatorial locale of Kilimanjaro, these penitentes point nearly straight upward. The size of the penitentes is approximately 40 cm from trough to peak. Picture taken by, and used with permission from, K.P. Hand.

Unlike Earth, Mars, and Pluto, the hard vacuum of Europa's exosphere prohibits any vapor accumulation layer near the surface. The dispersion relation breaks down without this vapor boundary layer, and penitente growth or decay on icy, airless worlds is not well described.

Lab experiments conducted by Bergeron et al. (2006) and Berisford et al. (2018) have successfully grown centimeter-scale penitentes inside cold thermal-vacuum chambers with low pressures and artificial light sources applicable to Earth conditions. However, experiments conducted by Berisford et al. (2021), in which pre-formed penitente analogs were placed in a hard-vacuum chamber, showed sublimation-driven erosion, yielding the decay and flattening of these analogs. However, unrealistically long experiment times prohibited the chamber from being run at the low (near 100 K) European temperatures observed by the *Galileo* spacecraft (Spencer et al., 1999)—a challenge to extending results to Europa.

A key mechanism behind penitente formation is radiative heat transfer (RHT) in the snow-like interior (Claudin et al., 2015). He and Flanner (2020) provide a comprehensive survey of RHT modeling in granular materials. RHT models begin with the RHT equation and focus on obtaining the spectral albedo and bidirectional reflectance of plane-parallel layers of snow, which are illuminated from above (He & Flanner, 2020). There are various numerical solutions to this problem, with the oldest and most rigorous being the discrete-ordinate-method radiative transfer theory (Chandrasekhar, 1960; Stamnes et al., 1988). Others include the two-stream approximation (Wiscombe & Warren, 1980), the adding-doubling method (Van de Hulst, 2012), the two-stream adding-doubling method (Briegleb & Light, 2007), and the approximate asymptotic radiative transfer theory (Kokhanovsky & Zege, 2004). More direct models use Monte Carlo methods (Tanikawa et al., 2006) or explicitly simulate photon interactions with clusters of ice grains (Kaempfer et al., 2007).

While these models agree quite well with experimental data under different circumstances, one challenge that remains unaddressed is RHT modeling of rough or irregular snow surfaces (He & Flanner, 2020; Warren, 1982), which is relevant to variable snow morphologies, and in particular to penitente formation. A surface roughness model by Lhermitte et al. (2014) uses view factor calculations to predict the penitente albedo for simple geometries. A computer model by Cathles et al. (2011) simulates the evolution of arbitrarily defined snow surfaces by assuming absorption and reflection at the surface and a uniform surface temperature equal to the melting point of water. A theoretical model by Tiedje et al. (2006) also solves for surface shape over time due to light diffusion in the snow and geometric focusing in the valleys. These models excluded internal light scattering and heat conduction, which are important mechanisms in penitente formation on Earth (Claudin et al., 2015), and in subsurface heating and spectral features of icy planetary surfaces (Matson & Brown, 1989).

To address shortcomings of experimental and modeling work in understanding penitente formation under vacuum conditions, we developed a computational model that simulates solar radiative warming of snow penitentes in a vacuum environment. The model can simulate RHT in irregular surfaces due to incident radiation by a moving direct light source, incorporating wavelength-dependent multi-scattering of photons in the granular interior and accounting for internal heat conduction. A model developed by Macias et al. (2023) complements our RHT model

Table 1
Description of Inputs to UTShine

Quantity	Description	Comments/Notes
t_F, N_t	(s) Final simulation time and the number of time steps	The initial time is $t_0 = 0$ s $\Delta t = t_F/N_t$ is the step size
W, H, L	(m) Domain width, height, and depth, respectively	–
$\{\mathbf{S}_j = (x_j, z_j)\}_{j=1}^{N_s}$	(m) Nodes that define the snow surface (snow-vacuum interface). Surface line segment j is defined by nodes $\mathbf{S}_j$ and $\mathbf{S}_{j+1}$	The nodes are defined at the $y = 0$ plane. The surface is extruded in the $+y$ direction by L to form the surface
$\theta(t)$, $\phi(t)$	(rad) Zenith and azimuth angles, respectively, of the Sun's trajectory over time in a spherical coordinate system	–
$I(\lambda)$	(W/m^2/m) Spectral flux emitted by the Sun (direct light) when $\theta = 0$	When $\theta \neq 0$, the Sun deposits a flux of $I(\lambda)\cos(\theta)$, following Lambert's cosine law
$\lambda_L \leq \lambda \leq \lambda_U$, N_λ	(m) Spectral range to be simulated, and segmentation of the spectrum into N_λ bins of equal width	Wavelength bin size is $\Delta\lambda = (\lambda_U - \lambda_L)/N_\lambda$
T_0	(K) Initial snow temperature (i.e., $T(t = 0, \mathbf{x}) = T_0$)	–
κ	(W/m/K) Snow thermal conductivity	Constant in space and time
ρ	(kg/m^3) Snow density	Constant in space and time
c_p	(J/kg/K) Snow constant-pressure specific heat	Constant in space and time
r	(m) Radius of the snow grains	Snow grains are uniformly distributed and identically spherical
$N_{\gamma,L}$	The number of solar photon bundles to simulate per time step	Photons are simulated in groups called bundles
$N_{\gamma,T}$	The number of thermal photon bundles to simulate per time step per snow surface segment	–
N_E	Discretize the snow medium into a computational mesh of approximately N_E elements	The mesh is discretized in 2D at the $y = 0$ plane and extruded in the $+y$ direction by L to convert to 3D

Note. Figure 2 illustrates select inputs. The following indices are consistently used throughout Section 2: i (bundle), j (surface node/segment), k (time), l (wavelength), m (mesh element), n (bundle step), and q (sample).

by simulating molecular transport over irregular surfaces that morph over time. In addition to understanding the mechanisms of penitente formation, our work may also help interpret *Galileo* and future observations of Europa and select safe landing sites for future spacecraft.

2. The Model

The model, called UTShine, is sufficiently generalized to simulate RHT due to any direct, incident light source (for instance, the Sun, light emitting diodes, or lasers) through irregular surfaces with a granular interior (for instance, snow or sand mixtures). While future work may explore additional applications, we will focus on describing UTShine and its application to pure water-ice snow morphologies on Europa. UTShine consists of the photon Monte Carlo solver (PMC) and the heat transfer solver (HT). PMC uses Monte Carlo methods to simulate internal light scattering and absorption by the snow interior. In contrast, HT uses the finite element method to solve the unsteady heat equation in the snow interior using the absorbed light energy computed by PMC. Let $t \in \mathbb{R}$ denote time and $\mathbf{x} = (x, y, z) \in \mathbb{R}^3$ denote a 3D position in physical space. Table 1 describes all inputs and outputs of UTShine, and 2 illustrates select inputs for further clarification.

For a given time step, PMC runs first, followed by HT. As illustrated in Figure 3, the solvers rely on the latest outputs from each other for initialization. For example, for time step $t_{k+1} \leq t \leq t_{k+2}$, PMC uses snow temperatures $T(t_{k+1}, \mathbf{x})$ calculated by HT to compute the thermal radiation emitted from the snow surface. Meanwhile, the heat sources $Q(t, \mathbf{x})$ calculated by PMC within $t_{k+1} \leq t \leq t_{k+2}$ are used by HT to compute the temperatures at t_{k+2}. Once the simulation finishes at t_F, UTShine returns the output quantities listed in Table 2. Figure 3 also shows how temperatures are defined at instants in time, while PMC outputs are piecewise constant. These differences are due to the different numerical methodologies used by PMC and HT, which we detail in Sections 2.1 and 2.2. Lastly, Section 2.3 applies the model to a case relevant to snow and ice morphologies on Europa. To ensure the model's fidelity, we check for numerical convergence and run tests that compare model outputs to theoretical and experimental data in Section Appendix A.

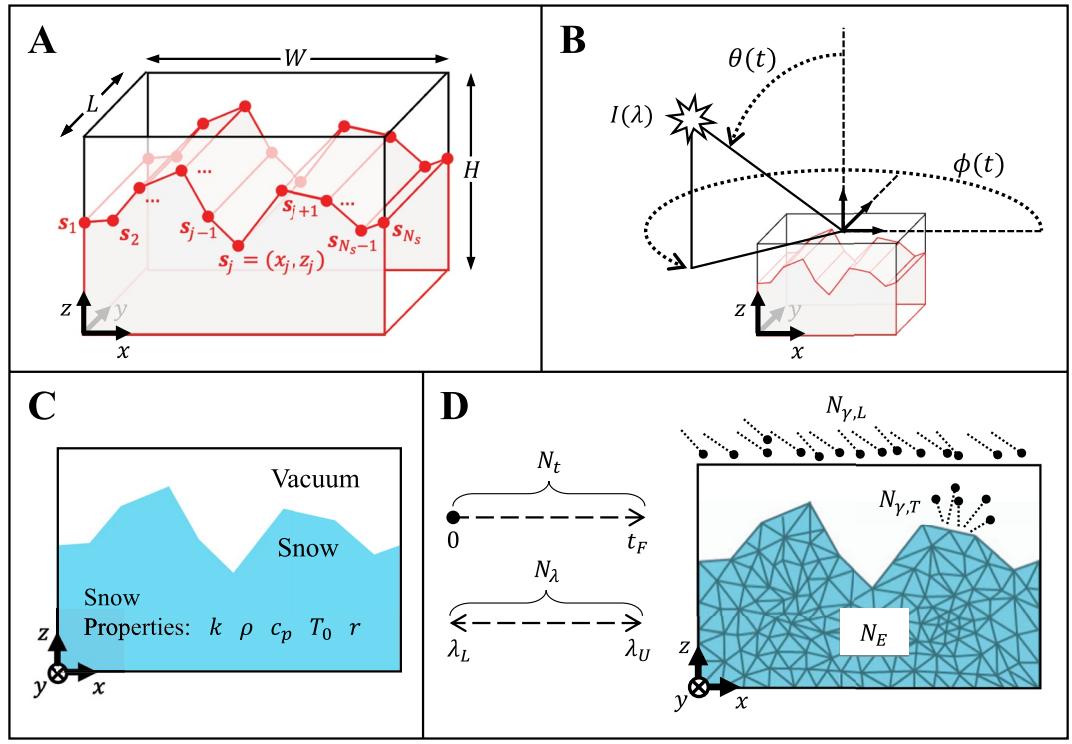

Figure 2. Relevant inputs to UTShine, described in Table 1. The inputs are categorized into four panels: (a) geometry, (b) illumination, (c) physical properties, and (d) numerical properties.

2.1. The Photon Monte Carlo Solver

Standard RHT modeling in snow and granular media typically involves obtaining numerical solutions to the RHT equation (He & Flanner, 2020), as described in Section 1; however, we take the Monte Carlo-based approach by mimicking the micro-interactions between light and snow in our computer model. This approach is intuitive and simpler to implement for the complex geometries under investigation. Tanikawa et al. (2006) and Kaempfer et al. (2007) have used microscopic modeling approaches for RHT modeling in snow. In a related application, Prem et al. (2019) developed a Monte Carlo RHT model for rarefied gases in Lunar atmospheres. This work builds on past approaches by accounting for irregular "self-viewing" surfaces and thermal surface emission.

As in Tanikawa et al. (2006) and Prem et al. (2019), the method implemented in PMC is based on Monte Carlo simulation, in which random samples are sequentially drawn from a variety of distributions to estimate output quantities via statistical averaging (Owen, 2013). To draw samples from these distributions, we use the inverse transform method (Devroye, 1986). For example, let $f_X(x)$ denote the (normalized) distribution of the quantity of interest, and let $F_X(x)$ denote its cumulative integral, which increases monotonically from 0 to 1. To draw a sample from $f_X(x)$, we first sample u_q from a uniform distribution between 0 and 1, then solve the inversion problem

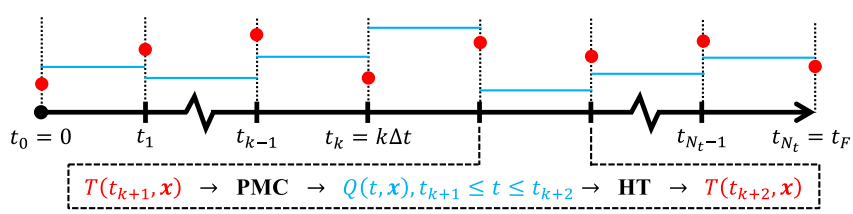

Figure 3. The algorithmic interaction between the photon Monte Carlo (PMC) and heat transfer (HT) solvers as the simulation evolves. $Q(t, \mathbf{x})$ and $T(t, \mathbf{x})$ are heat sources and temperatures, respectively, computed by PMC and HT. Additional outputs are listed in Table 2. Note that temperatures are defined at instant points in time (red dots), while outputs from PMC are piecewise constant (blue lines).

Table 2
Outputs From UTShine

Quantity	Description
$F_{\downarrow}(t, \lambda)$	(W/m^2/m) Incident Flux, solar energy entering through the domain ceiling, per unit time, per unit area, per unit wavelength. See Equation 16
$F_{\uparrow}(t, \lambda)$	(W/m^2/m) Reflected Flux, solar energy exiting through the domain ceiling, per unit time, per unit area, per unit wavelength. See Equation 16
$Q(t, \mathbf{x})$	(W/m^3) Volumetric Absorption, solar + thermal energy absorbed inside the snow per unit time, per unit volume. This quantity becomes a heat source for the heat equation. See Equation 14
$T(t, \mathbf{x})$	(K) Temperatures inside the snow over time

Note. Section 2.1.3 describes their calculation.

$x_q = F_X^{-1}(u_q)$. After repeating this procedure for $q = 1, 2, \ldots, N_q$, the values of x_q will be distributed according to $f_X(x)$ given a large enough N_q. In practice, $f_X(x)$ is known empirically (vs. analytically) without normalization. Therefore, $f_X(x)$ is normalized by its numerical integral before inverse sampling, and the inversion problem is solved using piecewise linear interpolation.

For the time interval $t_k \le t \le t_{k+1}$, PMC simulates groups of photons, called *bundles*, rather than physical photons for computational efficiency. Bundles emitted from the Sun, called solar bundles, enter through the ceiling boundary of the domain. In contrast, bundles emitted due to black body radiation, called thermal bundles, are launched from the snow surface. The bundles travel in straight paths in the vacuum region and follow a stochastic scattering/absorption algorithm inside the snow medium (detailed in Section 2.1.2). The side, front, and back domain boundaries are periodic, so bundles that escape through one boundary re-enter the opposite side. This periodicity mimics a snow field of infinite extent with a repeating surface pattern. The ceiling boundary is an outlet that allows bundles to exit while the floor boundary absorbs any incident bundles. The parallel code tracks millions of bundles as they randomly move in discrete physical steps within the domain. Tracking of a single bundle ends when either (A) less than 1% of the bundle's initial energy is left, (B) the bundle reaches the domain ceiling, or (C) the bundle is absorbed at the floor boundary. Upon tracking all bundles, PMC outputs (a) the absorbed energy in the snow, (b) the incident solar flux, and (c) the reflected solar flux (see Table 2). The following subsections detail how bundles are emitted, scattered, and absorbed.

2.1.1. Emission of Photon Bundles

Let λ_i, $\mathbf{r}_i^{(n)}$, $\mathbf{u}_i^{(n)}$, and $E_i^{(n)}$ denote, respectively, the wavelength, position, direction unit vector, and energy of photon bundle i at physical step n (wavelength is constant and hence does not use the superscript n). These properties are initialized during emission at $n = 0$. λ_i, $\mathbf{r}_i^{(n)}$, $\mathbf{u}_i^{(n)}$ are randomly sampled while $E_i^{(n)}$ is derived from λ_i and the number of photons per bundle, ρ_N. We first describe how ρ_N is calculated, then describe how other bundle properties are sampled and assigned. For solar bundles, ρ_N is computed as:

$$\rho_N = \frac{W \times L}{N_L} \int_{\lambda_L}^{\lambda_U} I(\lambda) \frac{\lambda}{hc} \, d\lambda \int_{t_k}^{t_{k+1}} \cos(\theta(t)) \, dt \tag{1}$$

$h = 6.626 \times 10^{-34}$ J-s is the Plank constant and $c = 2.998 \times 10^8$ m/s is the speed of light. The rightmost integral accounts for the intensity of the direct sunlight as it varies with the cosine of the zenith angle through time. The leftmost integrand converts the spectral irradiance, $I(\lambda)$, to a photon flux integrated across wavelengths. $W \times L$ is the area of the domain ceiling. In summary, Equation 1 states that, for a fixed number of light source bundles N_L, more photons are emitted when either (A) the domain is larger, (B) a wider spectrum of wavelengths are simulated, (C) a brighter light source defined by $I(\lambda)$ is used, (D) a longer time interval is simulated, or (E) the light source resides directly overhead more frequently.

A similar equation is computed to determine the number of thermal photons per bundle for a given surface segment j:

$$\rho_N = \frac{\Delta t \ \Delta A_j}{N_T} \int_{\lambda_L}^{\lambda_U} q_j(\lambda) \frac{\lambda}{hc} \, d\lambda \tag{2}$$

ΔA_j is the segment surface area (segment length times domain depth, L). $q_j(\lambda)$ is the spectral energy flux, which we compute using Plank's law, integrated over all solid angles in the hemisphere orthogonal to the surface segment:

$$q_j(\lambda) = \frac{2\pi hc^2}{\lambda^5} \frac{1}{e^{hc/(\lambda k_b T_j)} - 1} \tag{3}$$

$k_b = 1.381 \times 10^{-23}$ J/K is the Boltzmann constant. T_j is the surface temperature, which we compute by averaging node temperatures on the surface segment at time $t = t_k$. Note that Plank's law assumes local thermodynamic equilibrium (Planck, 1914), which is appropriate for this study given the time scale disparity between photon propagation ($O(10^{-8})$ s) and the Sun's motion ($O(10^5)$ s). Additionally, Equation 3 assumes unit emissivity since snow is highly absorptive (and therefore highly emissive by Kirchhoff's law of thermal radiation) at thermal infrared wavelengths (Wiscombe & Warren, 1980). In summary, Equation 2 states that, for a fixed number of thermal bundles, N_T, more photons are emitted when either (A) the surface segment is larger, (B) a wider spectrum of wavelengths are simulated, (C) a hotter flux defined by $q_j(\lambda)$ is used, or (D) a longer time interval is simulated.

λ_i is sampled from the distributions $I(\lambda)$ and $q_j(\lambda)$ for solar and thermal bundles, respectively. Since λ_i represents the wavelength of all photons in bundle i, the initial bundle energy, $E_i^{(0)}$, is computed as:

$$E_i^{(0)} = \rho_N \frac{hc}{\lambda_i} \tag{4}$$

$\mathbf{r}_i^{(0)}$ is sampled uniformly over each surface segment for thermal bundles and uniformly over the domain ceiling for solar bundles. For thermal bundles emitted from surface segment j, $\mathbf{u}_i^{(0)}$ is sampled from a Lambertian distribution normal to that surface segment. A Lambertian distribution describes the angular distribution of emitted energy from a perfectly diffusive surface, in which more energy is emitted orthogonal to the surface than at grazing angles. Given the rough microstructure of snow surfaces, a directionally diffusive emission model, such as the Lambertian distribution, is an accurate assumption for most viewing angles (Warren, 1982).

For solar bundles, $\mathbf{u}_i^{(0)}$ depends on the direction of the light source, which is time-dependent. Therefore, the launch time t_i is sampled from the distribution $\cos(\theta(t))$, $t_k \le t \le t_{k+1}$. This launch time is then used to calculate $\mathbf{u}_i^{(0)}$ as follows:

$$\mathbf{u}_i^{(0)} = -\sin(\theta(t_i)) \times \cos(\phi(t_i))\ \mathbf{i}\ \ -\sin(\theta(t_i)) \times \sin(\phi(t_i))\ \mathbf{j}\ \ -\cos(\theta(t_i))\ \mathbf{k} \tag{5}$$

$\mathbf{i}$, $\mathbf{j}$, and $\mathbf{k}$ denote the unit basis vectors in the x, y, and z directions, respectively.

2.1.2. The Scattering and Absorption Algorithm

Snow consists of grains of various shapes, sizes, and spatial distributions, which introduce challenges to modeling and simulating RHT. Furthermore, for purely water-ice snow, grain size and optical properties vary with temperature (Grundy & Schmitt, 1998) and with snow age (Warren, 1982). For simplicity in developing a light scattering and absorption algorithm, we assume snow grains are uniformly distributed, spherical, identically sized, and purely water-ice. While snow grains are not spherical, an effective spherical scattering symmetry may describe their random orientations and corresponding angular scattering distributions. By assuming uniformly distributed snow grains, the snow density, ρ, becomes spatially uniform. This idealized snow is optically representative of any water-ice snow with an equivalent volume-to-surface area ratio (Grenfell & Warren, 1999). For this scattering model, we use Mie theory (Mie, 1908) to derive the single-scattering behavior of an isolated, water-ice sphere, then use the delta-Eddington approximation (Wiscombe & Warren, 1980) to compute the *average* single-scattering behavior for ensembles of water-ice spheres comprising the snow medium. Mie scattering is appropriate for particles whose radius r is comparable to the wavelength of incident light λ. The scattering behavior depends on r, λ, and the refractive indices of the particle and surrounding environment. We use the wavelength-dependent refractive index of water-ice provided by Warren and Brandt (2008) and a unity refractive index for the vacuum environment.

From Mie theory, we obtain the single-scattering properties, namely the extinction efficiency Q_{ext}, the single-scattering albedo ω, and the asymmetry parameter g (Mätzler, 2002). We then use the delta-Eddington

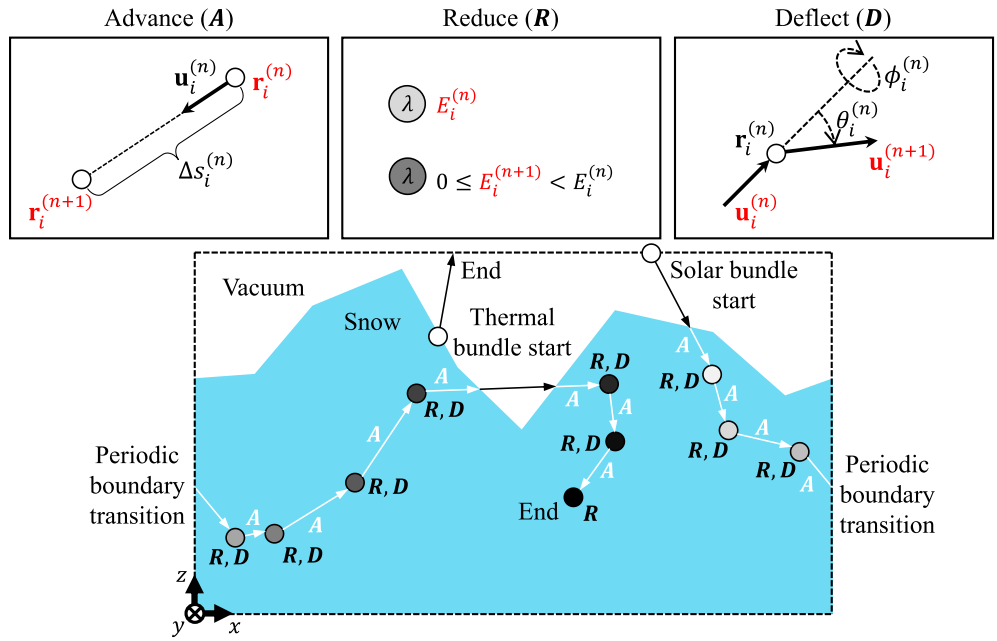

Figure 4. A schematic of the scattering and absorption algorithm (Section 2.1.2). A solar bundle starts at the ceiling, while a thermal bundle starts at the snow surface. Both bundles travel straight in the vacuum region. By chance, the thermal bundle heads toward the ceiling and exits. We darken the solar bundle as it moves through the snow to show its energy decreasing. Note that the bundles' paths reside in 3D space, and the above paths are projected onto the $x-z$ plane.

approximation to compute the *average* quantities (the attenuation coefficient μ^*, single-scattering albedo ω^*, and asymmetry parameter g^*):

$$\mu^* = \frac{3\rho}{4\rho_{\text{ice}}}\frac{Q_{\text{ext}}}{r}\left(1-g^2\omega\right) \tag{6}$$

$$\omega^* = \frac{\left(1-g^2\right)\omega}{1-g^2\omega} \tag{7}$$

$$g^* = \frac{g}{1+g} \tag{8}$$

where $\rho_{ice} = 917$ kg/m^3 is the density of water-ice at 273 K. On average, larger μ^*, ω^*, and g^* indicate more compact, absorptive, and diffusive snow.

Scattering and absorption are simulated using a Monte-Carlo-based algorithm developed by Jacques and Wang (1995) for turbid media. The algorithm requires as input μ^*, ω^*, and g^*. The Monte Carlo algorithm, which we illustrate in Figure 4, consists of three steps: *advance*, *reduce*, and *deflect*. When they first enter the snow, bundles follow the *advance* step. Since snow is microscopically rough and discontinuous, photons will travel on average a distance μ^* before their first interaction with a snow grain. Upon striking a snow grain, a fraction of the photons, dependent on ω^*, are absorbed (the *reduce* step), and the remainder is scattered (the *deflect* step) by an angle dependent on g^*.

In the *advance* step, we calculate a free-path distance and update the bundle position as follows:

$$\Delta s_i^{(n)} = -\frac{\ln\left(\xi_i^{(n)}\right)}{\mu^*} \tag{9}$$

$$\mathbf{r}_i^{(n+1)} = \mathbf{r}_i^{(n)} + \Delta s_i^{(n)} \times \mathbf{u}_i^{(n)} \tag{10}$$

$\xi_i^{(n)}$ is sampled from a uniform distribution between 0 and 1. In the *reduce* step, a fraction of the bundle's energy is removed and deposited in the triangular mesh element containing the bundle:

$$E_i^{(n+1)} = \begin{cases} \omega^* \times E_i^{(n)}, & \text{if } E_i^{(n)} > 0.01 E_i^{(0)} \\ 0, & \text{otherwise} \end{cases} \tag{11}$$

Lastly, we simulate scattering in the *deflect* step by sampling a polar angle $\theta_i^{(n)}$ and an azimuth angle $\phi_i^{(n)}$ relative to $\mathbf{u}_i^{(n)}$. $\phi_i^{(n)}$ is uniformly sampled from 0 to 2π radians, while $\theta_i^{(n)}$ is sampled from the Henyey-Greenstein scattering function (Henyey & Greenstein, 1941):

$$\theta_i^{(n)} = \cos^{-1}\left(\frac{1}{2g^*}\left[1 + (g^*)^2 - \left(\frac{1 - (g^*)^2}{1 + g^*\left(1 - 2\zeta_i^{(n)}\right)}\right)^2\right]\right) \tag{12}$$

$\zeta_i^{(n)}$ is sampled from a uniform distribution between 0 and 1.

Equation 12 provides an analytic sampling expression and accurately captures the angular dependence of snow scattering (see Appendix A2). A value of g^* close to unity indicates strong forward scattering, while a value close to zero indicates isotropic scattering. Using $\theta_i^{(n)}$ and $\phi_i^{(n)}$, the bundle's direction, $\mathbf{u}_i^{(n)} = u_x\mathbf{i} + u_y\mathbf{j} + u_z\mathbf{k}$, is updated to $\mathbf{u}_i^{(n+1)} = u'_x\mathbf{i} + u'_y\mathbf{j} + u'_z\mathbf{k}$ as follows (Jacques & Wang, 1995):

$$\begin{aligned} u'_x &= \frac{\sin\left(\theta_i^{(n)}\right)}{\sqrt{1-u_z^2}}\left[u_x u_z \cos\left(\phi_i^{(n)}\right) - u_y \sin\left(\phi_i^{(n)}\right)\right] + u_x \cos\left(\theta_i^{(n)}\right) \\ u'_y &= \frac{\sin\left(\theta_i^{(n)}\right)}{\sqrt{1-u_z^2}}\left[u_y u_z \cos\left(\phi_i^{(n)}\right) + u_x \sin\left(\phi_i^{(n)}\right)\right] + u_y \cos\left(\theta_i^{(n)}\right) \\ u'_z &= -\sin\left(\theta_i^{(n)}\right)\cos\left(\phi_i^{(n)}\right)\sqrt{1-u_z^2} + u_z \cos\left(\theta_i^{(n)}\right) \end{aligned} \tag{13}$$

2.1.3. Calculating the Output Quantities

As bundles propagate in the snow medium, the removed energy is deposited in the elements of the computational mesh. The deposited energies are converted into heat sources, $Q(\mathbf{x}, t)$, as follows:

$$Q(t, \mathbf{x}) \approx \frac{\Delta E_m}{(\Delta A_m \times L)\ \Delta t} \tag{14}$$

$$t_k \le t \le t_{k+1}, \qquad \mathbf{x} \in \Omega_m$$

ΔE_m is the total bundle energy deposited in a specific time interval in mesh element m that occupies the spatial region Ω_m. The volume of element m is its area ΔA_m on the $x - z$ plane, multiplied by its extrusion depth of L. This results in a heat source distribution that only varies with x and z, while the variation with y remains constant. After PMC finishes tracking all bundles, we compute the incoming and reflected flux as follows:

$$F_\downarrow(t, \lambda) \approx \frac{\Delta E_\downarrow}{(W \times L)\ \Delta t\ \Delta\lambda} \tag{15}$$

$$F_\uparrow(t, \lambda) \approx \frac{\Delta E_\uparrow}{(W \times L)\ \Delta t\ \Delta\lambda} \tag{16}$$

$$t_k \le t \le t_{k+1}, \qquad \lambda_l \le \lambda \le \lambda_{l+1}$$

$\Delta E_{\downarrow}$ ($\Delta E_{\uparrow}$) is the total solar bundle energy emitted (escaping) through the ceiling at specific temporal and spectral intervals. The ceiling area is $W \times L$.

2.2. The Heat Transfer Solver

Thermal conduction in snow occurs through adjacent snow grains, whereas convective and radiative heat transfer occurs in the spaces between the grains, posing challenges to modeling and simulation. For simplicity, these microscopic processes can be described by an effective thermal conductivity that varies with density (Sturm et al., 1997). Although snow density varies with temperature and grain properties (Warren, 1982), we constrain the problem to a uniform snow density for additional simplicity and for consistency with the constant-density assumption in PMC (see Section 2.1.2). Specific heat capacity also fluctuates with temperature (Kauzmann & Eisenberg, 1969). Since this work aims to demonstrate the capabilities of UTShine, we constrain the heat transfer problem to constant thermal properties and offload thermal variation to future studies.

HT computes temperatures in the snow region using MATLAB's partial differential equation (PDE) toolbox. Since $Q(t, \mathbf{x})$ remains constant with y (see the paragraph following Equation 14), the 3D thermal conduction problem may be reduced to 2D. The PDE toolbox is set up to solve the 2D, unsteady heat equation with constant thermal conductivity κ, density ρ, and specific heat c_p:

$$\rho c_p \frac{\partial}{\partial t} T(t, \mathbf{x}) = \kappa \nabla^2 T(t, \mathbf{x}) + Q(t, \mathbf{x}) \tag{17}$$

$$t_k \le t \le t_{k+1}, \qquad \mathbf{x} \in \Omega_{\text{snow}} \mid y = 0$$

$\Omega_{\text{snow}}|y = 0$ denotes the snow region sliced at the $y = 0$ plane. Initial temperatures at $t = t_k$ are set to $T(t_k, \mathbf{x})$ from the previous time step. The boundary conditions at the snow surface are prescribed heat fluxes that account for the emission of thermal bundles in a finite wavelength range:

$$-\kappa \nabla T = \left(\int_{\lambda_L}^{\lambda_U} q_j(\lambda) \, d\lambda \right) \hat{\mathbf{n}}_j \tag{18}$$

$$t_k \le t \le t_{k+1}, \qquad \mathbf{x} \in \partial\Omega_{\text{snow}} \mid x_j \le x \le x_{j+1}, \; y = 0, \; z_j \le z \le z_{j+1}$$

$\partial\Omega_{\text{snow}}$ denotes the boundary of the snow region, and the inequalities further constrain the boundary to surface segment j. $\hat{\mathbf{n}}_j$ is the outward-pointing unit vector, normal to surface segment j. $q_j(\lambda)$ is the spectral flux emitted from surface segment j (see Equation 3). The left and right domain boundaries are periodic:

$$T(t, \mathbf{x}_L) = T(t, \mathbf{x}_R) \tag{19}$$

$$t_k \le t \le t_{k+1}$$

$$\mathbf{x}_L = \{\partial\Omega_{\text{snow}} \mid x = 0, \; y = 0, \; 0 \le z \le z_1\}$$

$$\mathbf{x}_R = \left\{\partial\Omega_{\text{snow}} \mid x = W, \; y = 0, \; 0 \le z \le z_{N_s}\right\}$$

The periodicity mimics a snow field of infinite extent, which maintains consistency with periodic boundary conditions in PMC. The floor boundary is prescribed a zero-flux (adiabatic) boundary condition:

$$-\kappa \nabla T = 0 \tag{20}$$

$$t_k \le t \le t_{k+1}, \qquad \mathbf{x} \in \partial\Omega_{\text{snow}} \mid 0 \le x \le W, \; y = 0, \; z = 0$$

The PDE Toolbox calculates the final solution at $t = t_{k+1}$ using the finite element method. The snow region is discretized into N_E triangular mesh elements, where temperatures are defined at the mesh nodes. Note that this differs from PMC, in which the heat sources are defined at the element centroids (for usage in HT, heat sources are linearly interpolated at mesh nodes). The spatial discretization results in a system of ordinary differential equations (ODEs), which is time-integrated using a combination of adaptive and multistep methods (Shampine & Reichelt, 1997).

Table 3
Default Inputs to UTShine for Simulation of European Penitentes

Input	Value	Comments
t_F, N_t	$t_F = 4,536,000$ s, $N_t = 900$	$t_F = 15$ Europa days, 60 time steps per day
W, H, L	$W = 0.1$ m, $H = 1.6$ m, and $L = 1$ m	Domain dimensions are flush with the snow surface
$\{\mathbf{S}_j\}_{j=1}^{21}$	Sinusoidal surface, as shown in Figure 5. $H_p = 0.1$ m and $D_p = 1.5$ m	W is both the penitente width and domain width
$\theta(t)$, $\phi(t)$	See Equations 21 and 22	Figure 6, Panel b illustrates the path of the Sun
$I(\lambda)$	See Equation 24	We use Planck's law to mimic the solar spectrum
$\lambda_L \le \lambda \le \lambda_U$, N_λ	$0.4 \le \lambda \le 300$ μm, $N_\lambda = 1$	Spectral results are not explored in this study. However, N_λ is increased in Appendix A2 for validation purposes
T_0	110 K	–
κ	0.04 W/(m K)	–
ρ	105.2 kg/m^3	–
c_p	1100 J/(kg K)	–
r	1,000 μm	–
$N_{\gamma,L}$, $N_{\gamma,T}$	10^6 and 5×10^4 respectively	–
N_E	11,156 generated elements	–

Note. Table 1 describes the inputs to UTShine.

2.3. Model Setup for European Penitentes

This section describes the simulation case representative of penitentes on Europa. The case inputs in Table 3 are used throughout Section 3 by default unless otherwise stated. Given that molecular mean free paths in Europa's atmosphere are on the order of kilometers, and the simulated surfaces exhibit roughness on the order of meters, we justly apply our vacuum-based model.

The simulation time t_F is long enough for temperatures to reach equilibrium. The initial temperature T_0 is based on simplified energy balance calculations to approximate equilibrium surface temperatures. Since $Q(t, \mathbf{x})$ remains constant with y (see the paragraph following Equation 14), any value may be used for L. The default surface

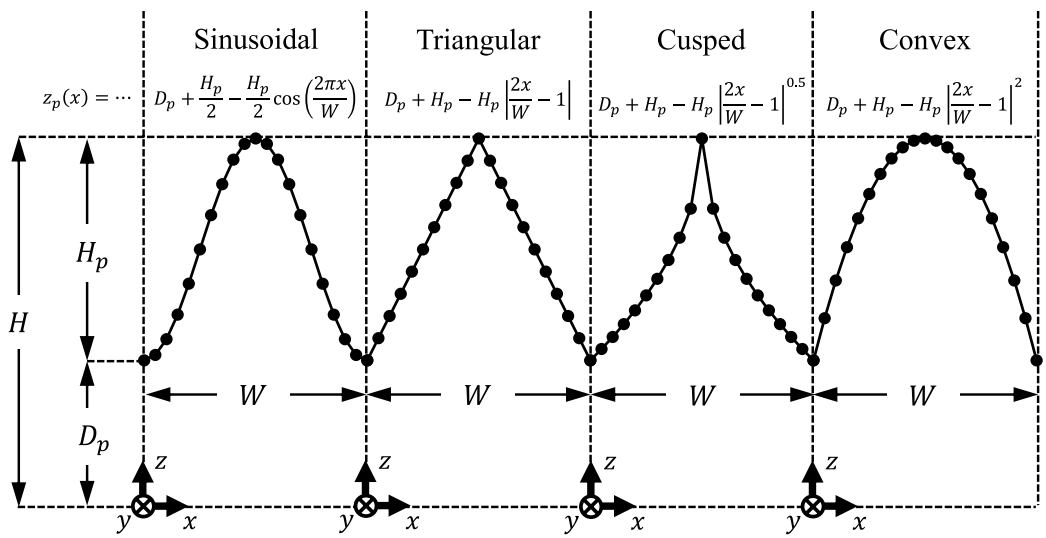

Figure 5. The four surface shapes used to represent penitentes, based on those by Lhermitte et al. (2014). The surface is composed of 21 surface nodes (20 surface segments) with equally spaced x coordinates from $x = 0$ to $x = W$. The corresponding z coordinates are described by $z_p(x)$. H_p and D_p are, respectively, the penitente height and depth below the valley. The domain height is $H = H_p + D_p$. W is both the penitente width and domain width.

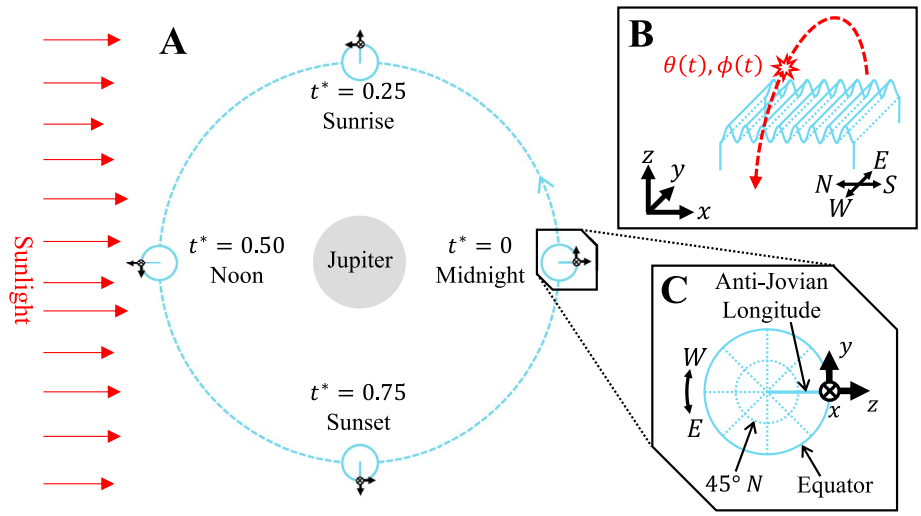

Figure 6. The solar path from different perspectives. (Panel a) Europa's orbit about Jupiter. $t^* \in [0, 1]$ (dimensionless) is Europa's normalized time of day. (Panel b) Solar path and its orientation relative to penitente ridges. When viewed orthogonal to the $x - z$ plane, the solar path appears as a vertical line centered at $x = W/2$. (Panel c) Location of the penitentes on Europa's far side, at the equator.

shape is sinusoidal since it yields surface temperatures between the extremes found in cusped and convex shapes (discussed in Section 3.3). The default penitente size is chosen to match the order of magnitude of Earthly penitente sizes (see Figure 1). The default snow depth below the lowest point on the surface is 1.5 m, which is the depth at which the daily temperature fluctuations become less than 1% of the temperature fluctuations present at the surface for a flat snow field (see Section 3.1).

As illustrated in Figure 6, the solar path is defined such that the penitentes are located at Europa's equator on the anti-Jovian longitude, with the surface ridges running East-West. The geolocation and orientation are consistent with that of Earthly penitentes (Bergeron et al., 2006; Betterton, 2001). Consequently, Jupiter and Jovian solar eclipses are not visible from this geolocation because Europa is tidally locked. To simplify the derivation of the solar path over time, we assume a circular orbit, zero axial tilt, and an orbital plane aligned with that of Jupiter:

$$\theta(t) = \pi |1 - 2\ t^*(t)| \tag{21}$$

$$\phi(t) = \begin{cases} \pi/2 & 0 \le t^*(t) \le 1/2 \\ 3\pi/2 & 1/2 < t^*(t) \le 1 \end{cases} \tag{22}$$

$$t^*(t) = \frac{t}{t_{\text{Europa}}} - \left\lfloor \frac{t}{t_{\text{Europa}}} \right\rfloor \tag{23}$$

$t_{\text{Europa}} = 3.024 \times 10^5$ s is the length of one Europa day, which is 3.5 Earth days. The floor function, $\lfloor \cdot \rfloor$, returns the greatest integer that is not greater than the input.

We approximate the Sun's spectral emission as a black body and use Planck's law integrated over all solid angles in a hemisphere (in units of W/(m^2 m)):

$$I(\lambda) = \left(\frac{R_{\text{Sun}}}{R_{\text{Jupiter}}} \right)^2 \frac{2\pi hc^2}{\lambda^5} \frac{1}{e^{hc/(\lambda k_b T_{\text{Sun}})} - 1} \tag{24}$$

$R_{\text{Sun}} = 6.95 \times 10^8$ m is the Sun's radius, $R_{\text{Jupiter}} = 7.7792 \times 10^{11}$ m is Jupiter's distance from the Sun, and $T_{\text{Sun}} = 5778$ K is the Sun's temperature. When integrated spectrally in the range used for simulation ($0.4 \le \lambda \le 300$ μm), Equation 24 yields an irradiance of about 44 W/m^2, which is 12% less than the maximum solar constant at Jupiter distance, 50 W/m^2 (Kopp & Lean, 2011).

The chosen spectral range balances physical accuracy and computational speed. It accounts for 99% of thermal emission from the snow surface at 100 K. Although simulating shorter wavelengths improves coverage of the solar spectrum, the scattering algorithm takes quite longer since snow becomes more transparent to shorter wavelengths of light (Wiscombe & Warren, 1980), resulting in over 10 million iterations per photon bundle. Computational costs decrease at longer wavelengths, where snow is highly absorptive. However, simulating longer wavelengths does not significantly impact solar or thermal energy coverage.

European snow is unlikely due to the lack of snowfall, though observations suggest that snow-like precipitation from water plumes is possible (Jia et al., 2018). To match thermal observations, we assume a snow surface. The thermal inertia $\left(\sqrt{\kappa \rho c_p}\right)$ at Europa's surface is 70 J/(m^2 K s$^{1/2}$) (Spencer et al., 1999). We obtain c_p = 1,100 J/(kg − K) from Kauzmann and Eisenberg (1969) for ice at a temperature of 120 K, which is consistent with Europa's equatorial temperatures (Spencer et al., 1999). Sturm et al. (1997) provide empirical relations between κ and ρ, which we use to obtain the correct thermal inertia. This results in $\kappa = 0.04$ W/(m K) and $\rho = 105.2$ kg/m^3, which describes a light and porous snow surface. In our simulations, we assume large snow grains ($r = 1{,}000$ μm), which aligns with the high porosity. This assumption also provides a computational speedup since larger snow grains are more absorptive (Wiscombe & Warren, 1980).

To aid in discussion throughout Section 3, we refer to the average albedo, a, which is defined as the fraction of solar energy reflected in one Europa day:

$$a = \frac{E_{\text{reflected}}}{E_{\text{in}}} \tag{25}$$

where

$$E_{\text{reflected}} = \int_{t_F - t_{\text{Europa}}}^{t_F} \int_{\lambda_L}^{\lambda_U} F_{\uparrow}(t, \lambda)\ d\lambda\ dt$$

$$E_{\text{in}} = \int_{t_F - t_{\text{Europa}}}^{t_F} \int_{\lambda_L}^{\lambda_U} F_{\downarrow}(t, \lambda)\ d\lambda\ dt$$

Section 3 also reports temperatures varying on the surface throughout the Europa day. These quantities are linearly interpolated in space. No temporal interpolation is necessary since the values are reported at exact time instants outputted by UTShine. We begin by analyzing a flat surface in Section 3.1 to provide intuition and comparison to published literature. Meanwhile, Sections 3.2–3.6 showcase results for more complex cases by systematically perturbing the default inputs and exploring their effects on penitente surface temperatures.

3. Results and Discussion

3.1. Properties of a Flat Snow Field

Figure 7 shows temperature versus depth throughout the day for two sets of snow density and thermal conductivity. The diurnal surface temperatures range from 85.6 to 113.01 K for light snow ($\rho = 105.2$ kg/m^3) and from 94.3 to 105.6 K for dense snow ($\rho = 400$ kg/m^3). The light snow yields daily temperatures more aligned with *Galileo* spacecraft observations (Spencer et al., 1999), which range from 85 to 130 K. Our simulations underestimate the daily high, partially because we do not cover the entire solar spectrum. Furthermore, calculations by Spencer et al. (1999) assume an albedo of 0.51, describing a snow-like surface with dirt and organic compounds. In contrast, our simulations yield an albedo of 0.61, which aligns with clear and pure snow. Consequently, our simulated penitentes receive and absorb less sunlight. The dense snow yields smaller daily temperature swings, which we expect due to its higher thermal inertia. The different thermal properties (lower κ, higher ρ, lower c_p) approximate those of old snow or solid ice (Sturm et al., 1997; Warren, 1982), which may be present on Europa. We thus consider rough surfaces with denser snow in Section 3.5.

The light penetration depth decreases significantly for dense snow, as indicated by the e-fold depth, d_e. (d_e is the depth at which the transmitted energy is a factor of e less than the incident energy at the surface.) At depths beyond 1.5 m, the transmitted energy becomes negligible (less than 1% of the incident energy). Denser snow

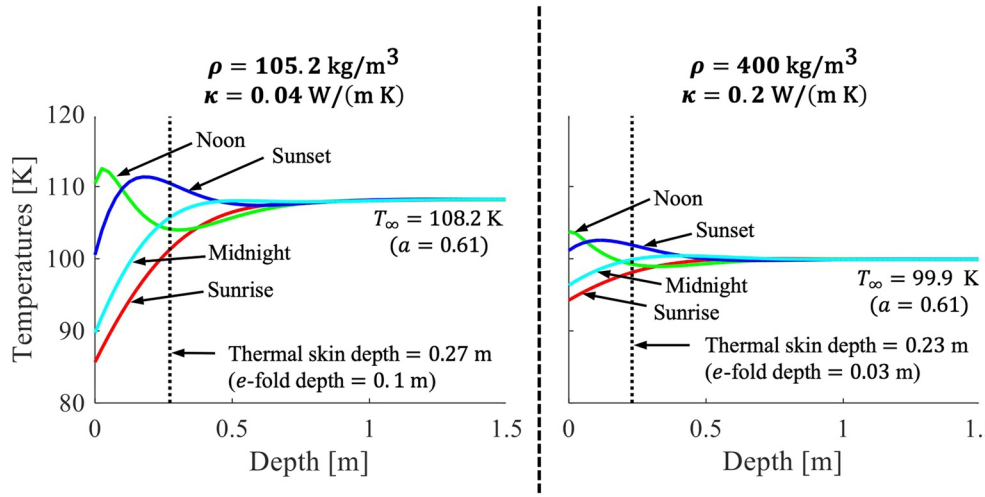

Figure 7. Temperatures versus depth at various times of day for two sets of snow density and thermal conductivity for a flat snow field. T_∞ is the (effectively static) snow temperature at a 1.5 m depth. a is the average albedo (Equation 25). The bold values above the plots are relevant inputs to UTShine. Other inputs are set to default values found in Table 3.

decreases d_e because the attenuation coefficient μ^*—a measure of how rapidly light dims inside a material—increases (see Equation 6). In terms of physics, densely packed snow scatters and absorbs photons faster, leading to a higher energy flux decrease over a given depth change.

The daily temperature changes are seen at greater depths for the light snow, as indicated by the thermal skin depths, d_T. (d_T is the depth at which temperature ranges are a factor of e less than at the surface.) Per Titus and Cushing (2012) and Matson and Brown (1989), larger thermal diffusivities ($\alpha = \kappa/(\rho \cdot c_p)$) and larger d_e cause an increase in d_T. In our simulations, α increases by $\sim 10^{-7}$ from light to dense snow. Simultaneously, d_e decreases by a factor of $\sim 10^{1}$, overpowering the effect of increasing α and resulting in a shallower d_T. Temperatures become static beyond a 1.5 m depth, which justifies using a depth of $D_p = 1.5$ m for more complex simulation cases (see Figure 5). At this depth, the internal temperature is 108 and 99.9 K for the light and dense snow, respectively. These differences can be explained by the volumetric heat capacity, $\rho \times c_p$, the heat source, $Q(t, \mathbf{x})$, and Equation 17. Although $Q(t, \mathbf{x})$ is identical, the dense snow warms at slower rates because there is more material per unit volume to warm up. Thus, slower warming prevents temperatures from reaching values achieved by the light snow.

The average albedo a (Equation 25) is identical for the light and dense snow, consistent with albedo calculations by Warren (1982), in which albedo is independent of density for snow of infinite depth. Our simulated snow is effectively infinite since less than 1% of light transmits through at a depth of $D_p = 1.5$ m. The independence of albedo on snow density is a scale-free phenomenon. From a geometric perspective, increasing ρ *at a constant grain size* decreases the photon mean free path by a factor C while keeping scattering angle distributions and absorption properties unchanged (Section 2.1.2). Therefore, the (average) path traced by a photon is scaled down by the same factor C from the light to dense snow. Since photon paths are proportionally equivalent, the fraction of escaping photons is equivalent, leading to identical albedos. Note that this scale-free phenomenon is only applicable to flat surfaces. For rough surfaces presented in the following sections, changing ρ affects where photons escape from (and re-enter) the snow after scaling their initial paths by C. This impacts the final photon fates and their contribution to the albedo.

3.2. Temperatures Versus Penitente Height

We begin with a nearly flat sinusoidal penitente surface and gradually increase H_p (see Figure 5). In Figure 8, the average albedo a decreases with taller sinusoids. For a flat snow surface, 100% of the photons that exit the snow exit the domain. As H_p increases, surface segments may "see" each other, and photons may re-enter the snow, in which they may be absorbed. This effect is amplified as penitentes become taller, which lowers albedo. The lower albedo also indicates more absorption, leading to an increase in T_∞.

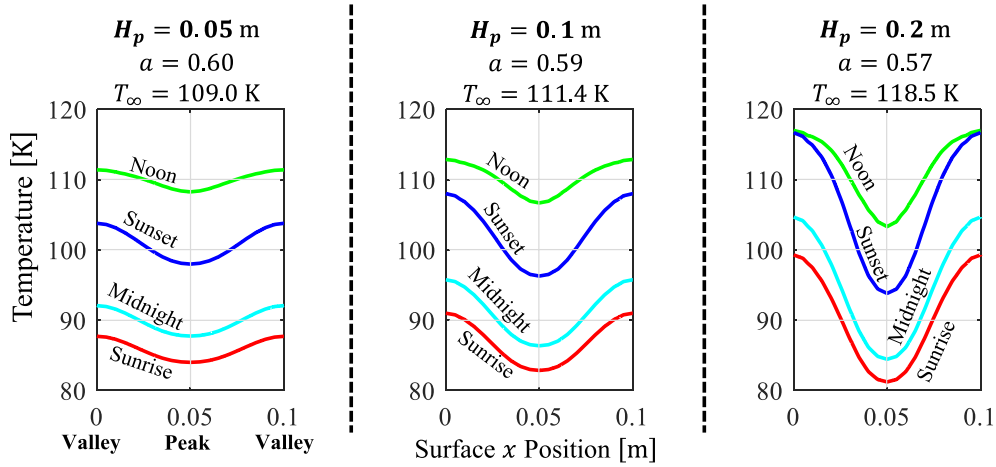

Figure 8. Surface temperatures at various times of day for different penitente heights. T_∞ is the (effectively static) snow temperature at a 1.5 m depth. a is the average albedo (Equation 25). The bold values above the plots are relevant inputs to UTShine. Other inputs are set to default values found in Table 3.

As H_p increases, the peak temperatures drop while the valley temperatures increase, which we attribute to geometric and thermal mechanisms. As seen in Figure 10 (leftmost column), solar absorption is nearly identical for the peaks and valleys, while thermal absorption is higher at the valleys. The net effect is more heat retention at the valleys than at the peaks, resulting in consistently hotter valleys throughout the day. For $H_p = 0.2$ m, this heat retention is high enough to keep the valleys at their noontime temperatures by the time the Sun reaches sunset.

Penitente growth primarily requires higher sublimation rates at the valleys compared to those at the peaks (Claudin et al., 2015), which occurs when valleys are sufficiently warmer than the peaks. In Macias et al. (2023), the required valley-peak temperature difference, δT, is a function of penitente shape and peak temperature. Using Equation 10 from Macias et al. (2023), as well as penitente heights and corresponding noontime peak temperatures presented in Figure 8, the required δT values are approximately 0.6 K ($H_p = 0.05$ m), 1.7 K ($H_p = 0.05$ m), and 2.6 K ($H_p = 0.05$ m). For all penitente heights, the simulated δT values exceed the threshold δT values, signifying potential penitente growth. However, additional factors, such as the actual composition of Europa's surface and the effects of sublimation, must be considered. This is the focus of future work. In Section 3.3, we explore the impact of penitente shape on the resulting temperature distribution and consequent δT.

3.3. Temperatures Versus Penitente Shape

This section discusses results for the surface shapes shown in Figure 5. Figure 9 shows the resulting surface temperature distributions. Temperatures are consistently higher at the valleys for all shapes throughout the European day. Notably, the cusped shape shows the greatest δT, which can be described by the solar and thermal energy absorption distributions (Figure 10). Solar energy absorption is highest at its flanks and valleys, contributing to higher warming rates in those regions. While most of its thermal energy is reabsorbed at the peak, the emitted thermal energy is not enough to reheat the peak.

Regarding the higher solar absorption by the cusped shape's flanks and valleys, we theorize that when sunlight strikes the cusped penitente's peak, solar photons enter at near-zero angles relative to the local surface and are briefly scattered before exiting to the flank and valleys of the penitente. This is in contrast to the convex shape, in which solar photons entering the peak strike at orthogonal angles relative to the local surface. Compared to the cusped shape, the flatter peak of the convex shape allows for more heat absorption and, consequently, warmer peaks, resulting in the lowest δT values across all surface shapes. The triangular and sinusoidal shapes exhibit temperature profiles and δT values nestled between the extremes of the cusped and convex shapes, with similar physical processes occurring.

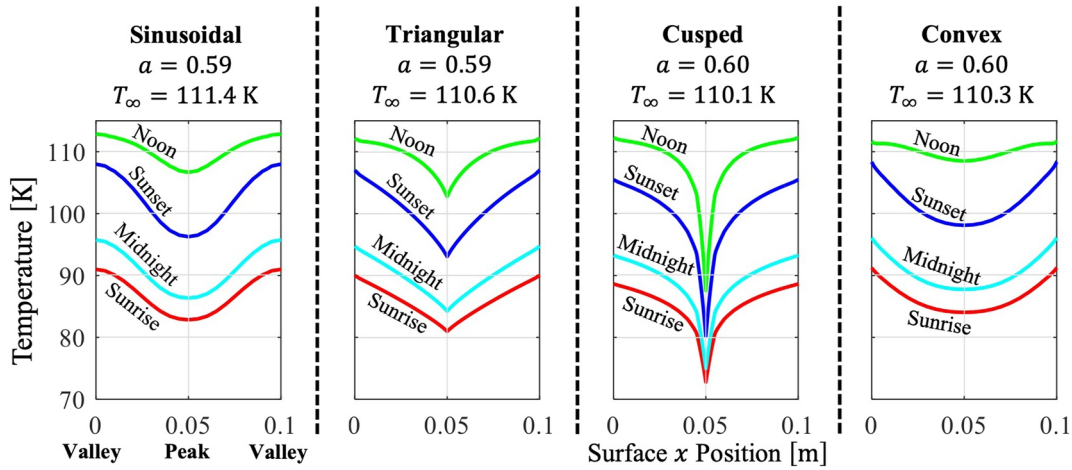

Figure 9. Surface temperatures at various times of day for different penitente shapes. T_∞ is the (effectively static) snow temperature at a 1.5 m depth. a is the average albedo (Equation 25). The bold values above the plots are relevant inputs to UTShine. Other inputs are set to the default values in Table 3. The penitente shapes are shown in Figure 5.

The simulated shapes suggest that sharper and narrower peaks are optimal for penitente growth since they yield larger δT values. In the Europa context, penitente growth depends on the initial surface roughness. Specifically, sharp and narrow penitente-like structures should be present at the centimeter scale to initialize penitente growth.

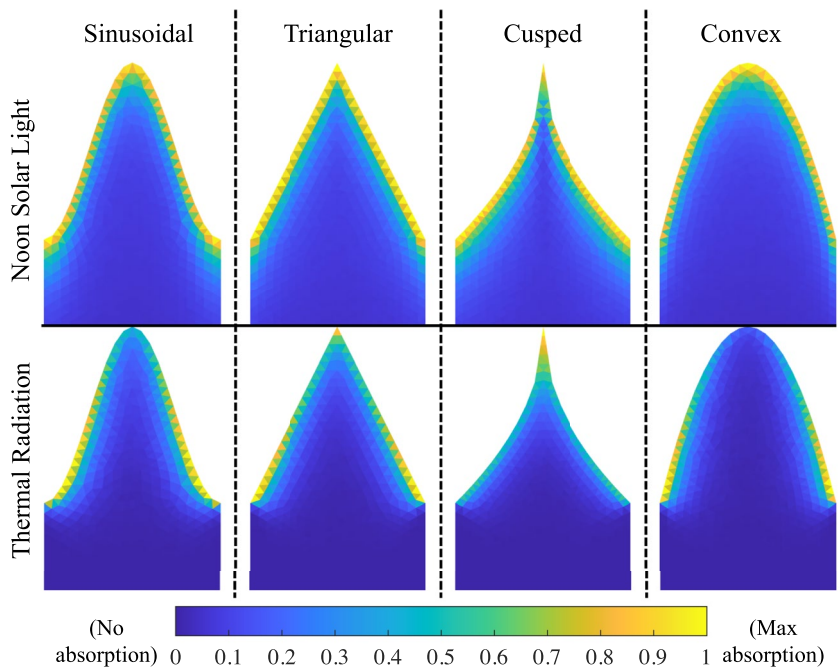

Figure 10. Normalized heat source sources of solar and thermal radiation for various surface shapes. To obtain heat sources exclusively from the Sun, we simulated a stationary sun at zero zenith and fixed surface temperatures to absolute zero to prevent thermal emission. In contrast, sole thermal heat sources are obtained by simulating a dark sky and fixing the surface temperatures to 100 K. Each heat source distribution $Q(t, \mathbf{x})$ (Equation 14) is normalized by its maximum value. Model inputs are set to default values found in Table 3.

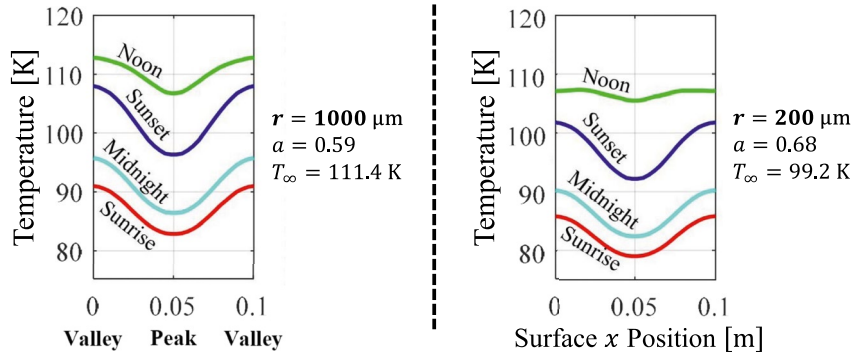

Figure 11. Surface temperatures at various times of day for different snow grain radii. T_∞ is the (effectively static) snow temperature at a 1.5 m depth. a is the average albedo (Equation 25). The bold values above the plots are relevant inputs to UTShine. Other inputs are set to default values found in Table 3.

3.4. Temperatures Versus Snow Grain Size

Figure 11 shows temperature distributions for two different grain radii. For the larger snow grain size of r = 1,000 μm, the average albedo is smaller, and T_∞ is higher. For larger snow grains, photons are mostly forward-scattered (see Section 2.1.2). Thus, for r = 1,000 μm, photons entering the snow travel mostly straight and deeper into the snow, increasing absorption and decreasing the average albedo a. The higher energy absorption also results in higher T_∞ values.

δT is larger throughout the day for r = 1,000 μm due to the higher solar photon absorption at the valleys. The forward-scattered photons entering at the peak are likely to either (a) continue traveling inward and below the valley height level or (b) escape through the flanks at a downward angle and re-enter through the valleys. In either case, photon absorption is likely below valley height. Therefore, photons are primarily absorbed in the valleys, even if they enter through the peaks. For r = 200 μm, photons are mostly side-scattered near the surface and diffuse almost uniformly, resulting in uniform heat sources and surface temperatures. From these results, penitente growth is likely for snow-like surfaces with larger grains. On Europa, *Galileo* results indicate that grain sizes in the range of 10–100 μm (Carlson et al., 2009), but sintering induced by daily cooling-warming cycles may lead to larger grains in some regions (Molaro et al., 2019).

3.5. Temperatures Versus Thermal Properties

Figure 12 shows surface temperature profiles for a light (low ρ and κ values) and dense snowpack. Note that the chosen thermal property sets are identical to those used in the flat snow simulations (Section 3.1), which we argued are relevant for studying European penitentes. δT is higher throughout the day for light snow, corre-

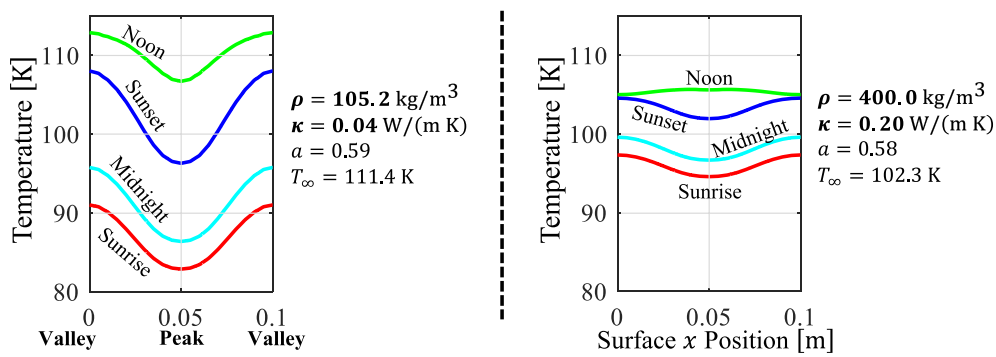

Figure 12. Surface temperatures at various times of day for different sets of thermal properties, which represent light (left) and dense (right) snow. T_∞ is the (effectively static) snow temperature at a 1.5 m depth. a is the average albedo (Equation 25). The bold values above the plots are relevant inputs to UTShine. Other inputs are set to default values found in Table 3.

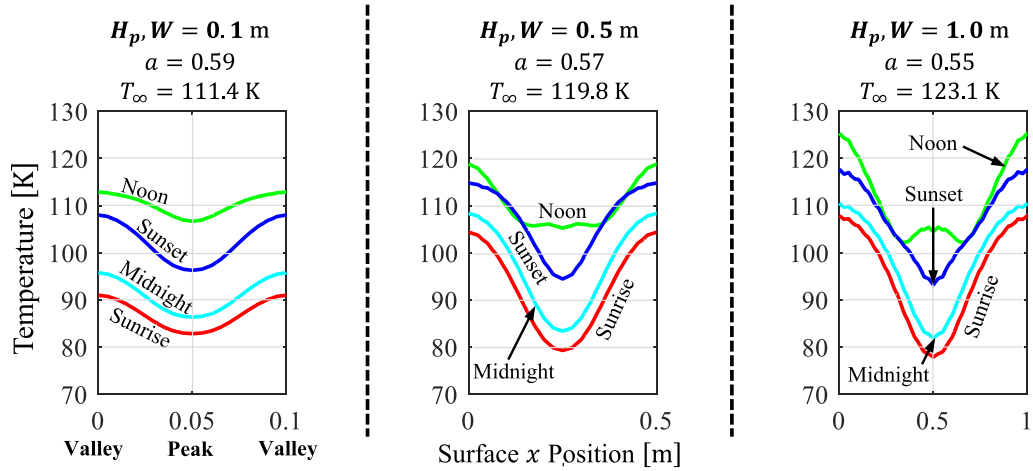

Figure 13. Surface temperatures at various times of day for different penitente sizes. T_∞ is the (effectively static) snow temperature at a 1.5 m depth. a is the average albedo (Equation 25). The bold values above the plots are relevant inputs to UTShine. Other inputs are set to default values found in Table 3.

sponding to lower thermal inertia. While the average albedos a are nearly identical, the light snow has a higher T_∞ value. The physical mechanisms at play are similar to those described in Section 3.1 and explain the observed δT, a, and T_∞ values. For dense snow, the peak briefly becomes warmer than the valleys at the solar zenith, which can be described by the optical depth and heat sources. As with the flat snow simulations, the optical depth is significantly shallower for the dense snow, which results in energy absorption occurring at greater concentrations in a thinner depth closer to the surface. Because of the smaller amount of snow mass present in the peak region compared to the valleys, this results in more significant temperature increases at the peaks. Results from Figure 12 suggest that lighter snow-like penitentes are better suited for growth on Europa due to their higher δT values.

3.6. Temperatures Versus Penitente Scale

Figure 13 shows the surface temperatures for three different penitente sizes. The largest penitente ($H_p = 1$ m) becomes warmest at its peak compared to its flanks, producing a "W" shape in the surface temperature distribution. This is likely due to its light penetration depth (and absorption depth) being proportionally smaller for the largest penitente, which causes a heat absorption spot at the peak at noon. δT increases with penitente size, suggesting that penitente growth may accelerate as the penitente size increases. However, according to Macias et al. (2023), the required δT for penitente growth increases with penitente size. To further extrapolate the effects of penitente size on δT, we must consider dynamical surface morphologies, peculiar temperature profiles such as the "W" temperature profile, and sublimation effects not present in this study.

4. Conclusions

We introduced UTShine, a new RHT model for simulating light scattering in granular media with irregular surfaces. UTShine consists of two interacting solvers: PMC (Section 2.1) and HT (Section 2.2). After investigating numerical convergence and physical validity (Appendix A), we applied UTShine to cases that are representative of Europa's environment (Section 2.3).

Results for a flat snow surface are consistent with findings by Warren (1982) and Spencer et al. (1999). Specifically, albedo is independent of density, and increasing density decreases the optical e-fold depth. Daily temperatures also align with *Galileo* spacecraft observations of Europa's equatorial temperatures (Spencer et al., 1999). Subsequent UTShine cases focused on the surface temperatures of sinusoidally shaped surfaces and the dependence on penitente height, surface shapes besides sinusoidal, snow grain size, thermal properties, and overall

penitente size. The key quantity of interest is the valley-peak temperature difference δT since warmer troughs promote penitente growth (Macias et al., 2023).

Results reveal that taller, narrower, and sharper surfaces yield larger δT values and warmer surfaces overall. The surface sharpness significantly increases δT, particularly at high noon (Section 3.3). Increasing snow grain size also increases δT and the daily surface temperatures (Section 3.4). Furthermore, surfaces with lower thermal inertia significantly increase δT and experience wider daily temperature swings (Sections 3.1 and 3.5). The case with higher thermal inertia yielded peaks warmer than the troughs near high noon, which is the only case that exhibited this behavior. Finally, larger penitentes result in larger δT values throughout the day (Section 3.6).

This study suggests that penitente growth is possible in Europa-like conditions near the equator for taller, larger, narrower, and sharper structures with coarse snow-like interiors and lower thermal inertias. Note that we made several simplifying assumptions throughout Section 2, with key assumptions being (a) thermal properties are constant in space and time, (b) snow is composed of identical water-ice grains with uniform distribution, and (c) only ~88% of the solar spectrum is simulated. Future work will address these assumptions and consider the joint effect of sublimation and other physics by using the models developed by Macias et al. (2023) for more realistic Europa applications.

Appendix A: Model Validation

A1. Numerical Convergence

Here, we investigate numerical convergence to ensure that numerical artifacts are not obscuring the model's outputs. Although there are five numerical inputs to UTShine (illustrated in Figure 2, Panel d), we only investigate the number of time steps, N_t, and the number of mesh elements, N_E, since they may have the most significant impact on the primary quantity of interest in this study: surface temperatures. While the number of bundles ($N_{\gamma,L}$ and $N_{\gamma,T}$) affects the noise levels present in the heat sources, this noise tends to be eliminated by the diffusive mechanisms inherent in conductive heat transfer. On the other hand, the number of spectral bins, N_λ, has no algorithmic effect on the output surface temperatures, which only depend on heat sources (see Equation 14).

To check for numerical convergence, we performed simulations with the default inputs found in Table 3 while varying either N_t or N_E separately. Furthermore, to check for Monte Carlo statistical convergence, we ran two identical simulations to ensure the output surface temperatures are nearly identical. Figure A1 shows the surface temperatures throughout the day for two simulation runs with identical inputs. The percent error difference (PED) at a specific x position on the snow surface, x_j, at time t_k is found as:

$$PED(x_j, t_k) = \frac{|T_2(x_j, t_k) - T_1(x_j, t_k)|}{T_1(x_j, t_k)} \times 100 \tag{A1}$$

where $T_1(x_j, t_k)$ and $T_2(x_j, t_k)$ refer to temperatures from two different simulation runs. The maximum PED is less than 1%, indicating statistical convergence. Figures A2 and A3 show surface temperatures throughout the day for varying N_t and varying N_E, respectively. The PED is less than 1% in both figures, indicating numerical convergence (Figure A3).

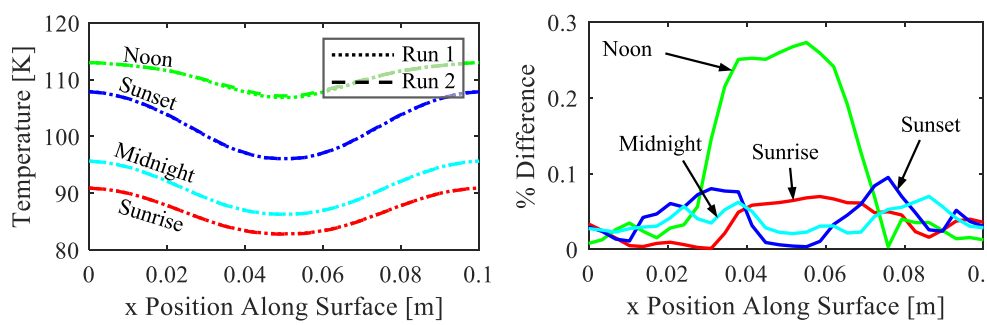

Figure A1. Statistical convergence of two simulations with identical inputs. Model inputs are set to default values found in Table 3. The PED (Equation A1) is less than 1%, and temperatures are visibly indistinguishable in the left plots.

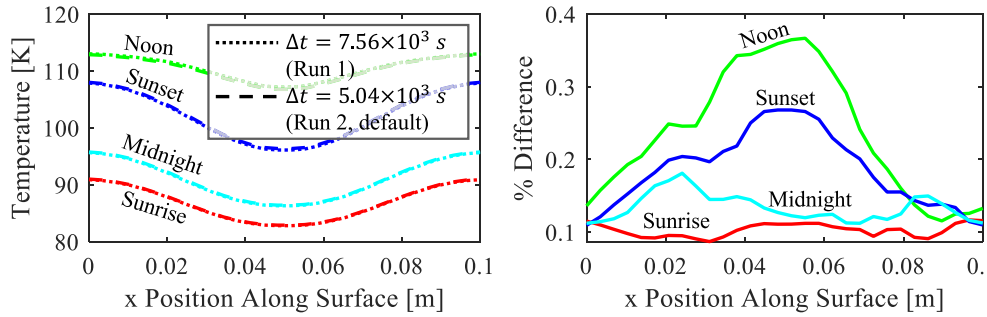

Figure A2. Numerical convergence of two simulations with a varying number of time steps, N_t. Δt is the time step size. Model inputs are set to default values found in Table 3. The PED (Equation A1) is less than 1%, and temperatures are visibly indistinguishable in the left plots.

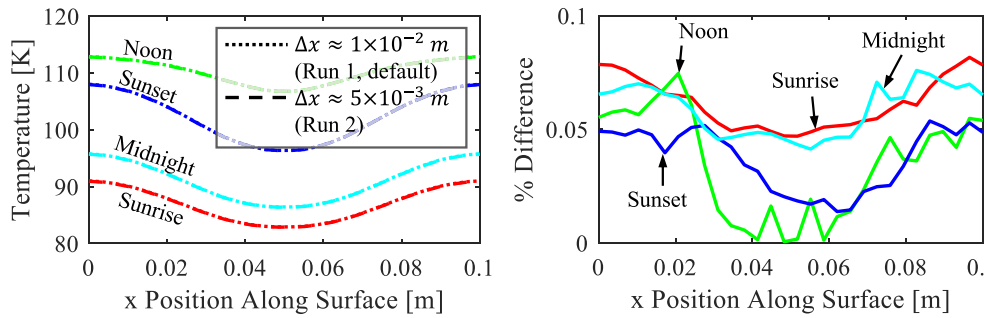

Figure A3. Numerical convergence of two simulations with a varying number of mesh elements, N_E. Δx is the approximate side length of a single triangular mesh element. Model inputs are set to default values found in Table 3. The PED (Equation A1) is less than 1%, and temperatures are visibly indistinguishable in the left plots.

A2. Spectral Albedo Versus Grain Size

This section tests the relationship between grain size and spectral albedo on a flat snow surface, using simulations with a fixed zenith angle and two different snow grain radii. Table A1 lists the inputs to UTShine for this validation case. To compute spectral albedo, we divide the reflected spectral energy by the incoming spectral energy:

Table A1
Relevant Inputs to UTShine for Simulation of Spectral Albedo

Input	Value	Comments
t_F, N_t	$t_F = 1$ s, $N_t = 1$	–
W, H, L	$W = 1$ m, $H = 1.1$ m, and $L = 1$ m	–
$\mathbf{S}_1$, $\mathbf{S}_2$	$\mathbf{S}_1 = (0, 1)$, $\mathbf{S}_2 = (1, 1)$	The surface is flat, with 0.1 m spacing between the surface and domain ceiling
$\theta(t)$, $\phi(t)$	$\theta(t) = 60° \times \pi/180$, $\phi(t) = 0$	We simulate a static light source
$I(\lambda)$	$\lambda/(hc)$ (W/(m^2 m))	Constant photon emission across all wavelengths
$\lambda_L \le \lambda \le \lambda_U$, N_λ	$0.4 \le \lambda \le 2.4$ μm, $N_\lambda = 200$	–
r	200, and 1,000 μm	We simulate two different grain sizes
$N_{\gamma,L}$, $N_{\gamma,T}$	10^7 and 0 respectively	Since we are interested in the reflected flux from incoming light, we omit the simulation of thermal bundles from the surface

Note. Table 1 describes the model inputs.

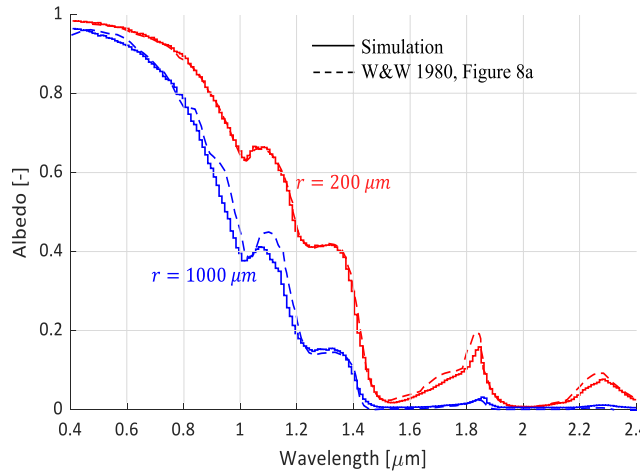

Figure A4. Model comparison against Wiscombe and Warren (1980) of snow spectral albedo at different grain radii, r, at a zenith angle of 60°. Model inputs are found in Table A1.

$$a(\lambda) = \frac{\int_0^{t_F} F_{\uparrow}(t,\lambda)\ dt}{\int_0^{t_F} F_{\downarrow}(t,\lambda)\ dt} \tag{A2}$$

$F_{\uparrow}$ and $F_{\downarrow}$ are the reflected and incident fluxes, respectively (see Table 2). Results are displayed in Figure A4, in agreement with Wiscombe and Warren (1980). Minor discrepancies are present in $0.8 \leq \lambda \leq 1.2$ μm for r = 1,000 μm and in $1.6 \leq \lambda \leq 1.9$μm for r = 200μm, which we attribute to differences in Mie calculations. Wiscombe and Warren (1980) explain that the single-scatter properties, a function of λ, are averaged over a small range of grain radii for a given grain radius to remove ripples present in the plots of single-scattering properties versus λ, but the details are left unclear. We remove these ripples by averaging grain radii that are 5% smaller and larger than the grain radius of interest. The remaining ripples are removed by smoothing the data points with a regression curve.

A3. Steady-State Temperature Predictions Following an Energy Balance

To validate the combined PMC and HT solvers, we compare the simulated steady-state temperatures of a flat scattering medium to those obtained analytically. Table A2 lists the inputs to UTShine. The assigned μ^*, ω^*, and g^* produce an optically thick medium that traps all incoming light (see Section 2.1.2). At equilibrium, we expect the absorbed incident energy ($E_{in} = 50(1-\alpha)\cos\theta$) to match the thermal energy emitted from the surface ($E_{out} = \sigma T^4$). Setting $E_{in} = E_{out}$ and solving for T leads to the equilibrium temperature as a function of θ:

$$T_{\text{equilibrium}}(\theta) = \left(\frac{50}{\sigma}(1-\alpha)\cos\theta\right)^{1/4} \tag{A3}$$

$\sigma = 5.67 \times 10^{-8}$ W/(m^2 K^4) is the Stefan-Boltzmann constant, and $\alpha = f(\theta, \mu^*, \omega^*, g^*)$ is the surface albedo, which we compute using formulas by Wiscombe and Warren (1980). Figure A5 shows $T_{\text{equilibrium}}$ versus $\cos(\theta)$, calculated using Equation A3 and computed from simulation, showing excellent agreement.

Table A2
Relevant Inputs to UTShine for Simulation of Thermal Equilibrium

Input	Value	Comments
t_F, N_t	$t_F = 60$ s, $N_t = 240$	60 s is found to be sufficiently long for temperatures to reach equilibrium from the initial temperature, $T_0 = 150$ K
W, H, L	$W = 1$ m, $H = 1.1$ m, and $L = 1$ m	–
$\mathbf{S}_1$, $\mathbf{S}_2$	$\mathbf{S}_1 = (0, 1)$, $\mathbf{S}_2 = (1, 1)$	The surface is flat, with 0.1 m spacing between the surface and domain ceiling
$\cos(\theta(t))$	0.1, 0.2, …, 0.9, 1.0	We simulate a static light source at various fixed zenith angles
$\phi(t)$	0 for all time	–
$I(\lambda)$	50 W/(m^2 m)	Constant energy emission at all wavelengths
$\lambda_L \leq \lambda \leq \lambda_U$, N_λ	$1 \leq \lambda \leq 2$ m, $N_\lambda = 1$	The spectral range is set such that $I(\lambda)$ integrated from λ_L to λ_U equals 50 W/m^2
r	None	In general, r is used to calculate μ^*, ω^*, and g^* (see Section 2.1.2). However, for this validation case, μ^*, ω^*, and g^* are set manually to analytically compute albedo using formulas by Wiscombe and Warren (1980)
μ^*	10^4 m^{-1}	–
ω^*	0.9	–
g^*	0.9	–
T_0	150 K	–
κ, ρ, c_p	All set to unity	Per Equation 17, these thermal values only affect the time to reach equilibrium, not the final surface temperature itself
$N_{\gamma,L}$, $N_{\gamma,T}$	10^7 and 0 respectively	Since we are interested in the reflected flux from incoming light, we omit the simulation of thermal bundles from the surface
N_E	2,492 generated elements	–

Note. Table 1 describes the model inputs.

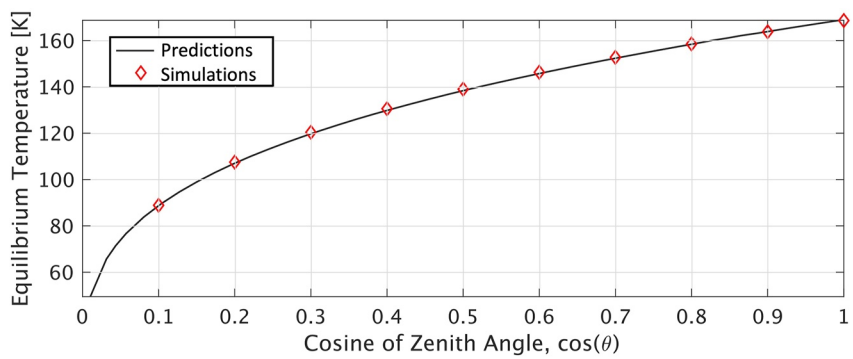

Figure A5. Model comparison against predictions of steady-state equilibrium surface temperatures (Equation A3). Each diamond is a different simulation at a fixed zenith angle. Simulation inputs are found in Table A2.

A4. Intensity of Back-Scattered Light From Penitentes

The last validation case replicates the reflected light distribution of a lab-made penitente field using a picture (from Berisford et al. (2021)) taken from a bird's eye. See Figure A6 for a CAD model of the chamber, the camera location, and the simulation setup. Simulation inputs replicating the setup are found in Table A3. Note that only the red channel of the picture is used for validation. Berisford et al. (2021) describes that the blue channel of the image is saturated due to camera calibration issues at cryogenic temperatures. The code to UTShine was modified so that (a) the ceiling boundary is divided into 100 segments to spatially resolve the reflected energy distribution, and (b) only photon bundles escaping near an angle of $\sim\beta = 67°$ (from Figure A6) are captured (Figure A7).

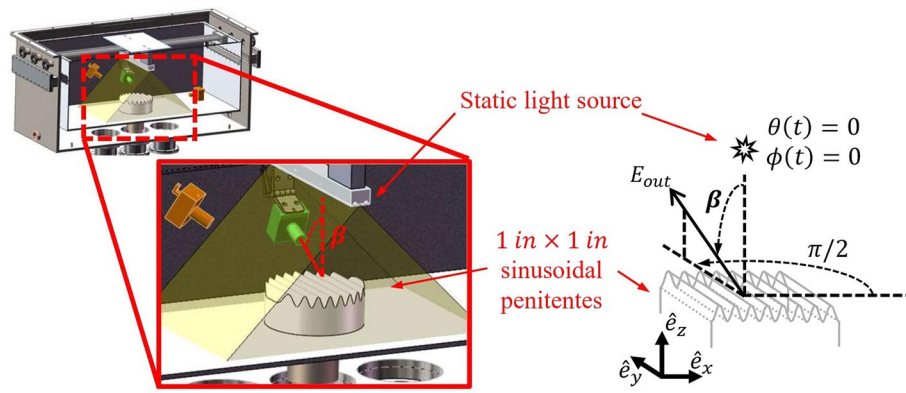

Figure A6. The cryogenic vacuum chamber setup from Berisford et al. (2021) and our model setup to closely match the experiment. The camera's line of sight is at $\sim\beta = 67°$ relative to the zenith, and the static LED light source is directly above. Simulation inputs are found in Table A3. During simulation, we record bundle energy, E_{out}, exiting at angles close to β to obtain back-scattered light intensity distributed over the penitente field. We compare this distribution against that captured by the camera in the vacuum chamber.

Table A3
Relevant Inputs to UTShine for Simulating Reflected Light Distributed Over a Sinusoidal Penitente Field for Comparison Against Experimental Data Found in Berisford et al. (2021)

Input	Value	Comments
t_F, N_t	$t_F = 1$ s, $N_t = 1$	–
W, H, L	$W = 1''$, $H = 3''$, and $L = 1$ m	–
$\{\mathbf{S}_j\}_{j=1}^{31}$	Sinusoidal surface, as shown in Figure 5. $H_p = 1''$ and $D_p = 2''$	–
$\theta(t)$, $\phi(t)$	$\theta(t) = 0°$, $\phi(t) = 0°$	A static light source directly above the snow
$I(\lambda)$	LED light source from Berisford et al. (2021)	Figure A7 shows a plot of $I(\lambda)$
$\lambda_L \leq \lambda \leq \lambda_U$, N_λ	$0.6 \leq \lambda \leq 0.7$ μm, $N_\lambda = 1$	Red light. Only the red picture channel is used for validation
ρ	300 kg/m^3	This value is the measured snow density in Berisford et al. (2021)
r	1,000 μm	The snow gradually warmed and sintered during the experiment, justifying the larger snow grain size
$N_{\gamma,L}$, $N_{\gamma,T}$	10^7 and 0 respectively	Since we are interested in the reflected flux from the incoming LED light, we omit the simulation of thermal bundles from the surface

Note. Table 1 describes the model inputs.

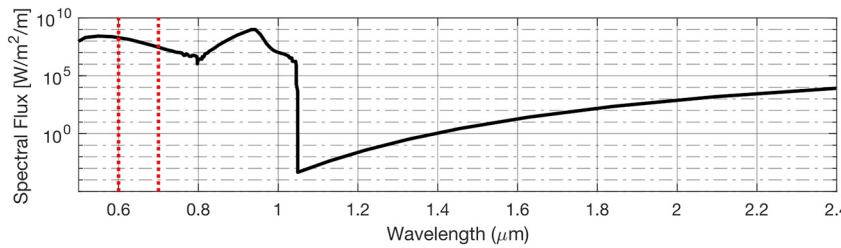

Figure A7. Spectral flux from the LED bar recorded at the surface of the snow sample from Berisford et al. (2021). We simulate wavelengths between the dashed vertical lines, $0.6 \leq \lambda \leq 0.7$ μm. Other simulation inputs are found in Table A3.

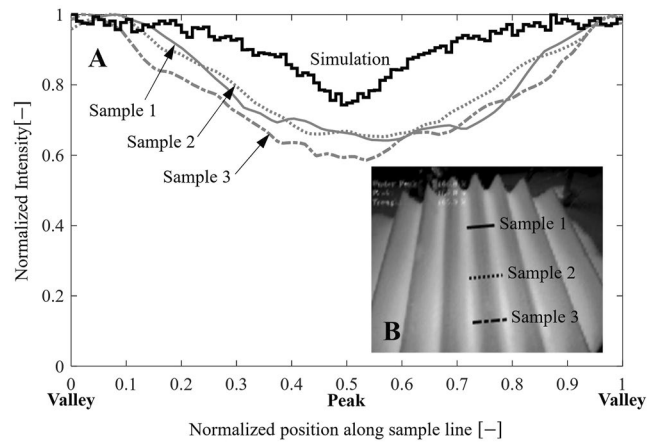

Figure A8. Model comparison against Berisford et al. (2021) of red light reflected from a snow penitente field toward a bird's eye view camera. For simulation, we only captured light that escapes at angles close to ∼67° from the vertical. See Figure A6 for the model geometry and experimental setup.

The distribution of light exiting the simulation domain is compared to sample lines from the picture. Results are shown in Figure A8. The intensities are normalized since absolute intensity data cannot be easily extracted from the RGB values of a picture. The simulated and experimental intensities are in agreement toward the valleys; however, simulated intensities are brighter toward the peak. We attribute these discrepancies to view angle effects, which is a limitation of the pseudo-3D setup of UTShine. Because the camera's distance from the penitente field is close to the same order of magnitude as the size of the penitente field, the camera receives light from a wider range of angles. In contrast, the simulation records light escaping at an acute exit angle, β. Note that only a tiny fraction of red photon bundles escape from the snow, and a smaller sub-fraction escape at angle β through the ceiling boundary. Therefore, most bundles do not contribute to the final solution, resulting in the noise seen in the solid black line.

Data Availability Statement

The picture seen in Figure 1, as well as the LED spectral data presented in Figure A7, are available via Figshare (Carreon, 2023a, 2023b). The picture presented in Figure 1 was captured by K.P. Hand. Schematics in Figure 2 through Figures 6 and A6 were produced using PowerPoint. Pictures in Figures A6 and A8 and the LED spectrum plotted in Figure A7 were obtained with permission from experiments conducted by Berisford et al. (2021) at the Jet Propulsion Lab. The data from Wiscombe and Warren (1980) plotted in Figure A4 was extracted using the WebPlotDigitizer tool (Rohatgi, 2022). All plots were produced using MATLAB. Due to ongoing research

and dissertation work related to UTShine by Ph.D. students A. Carreon and A. Macias, the code and raw data are currently unavailable. However, in compliance with the FAIR reporting procedures and requirements, we have detailed all equations and logical processes necessary to reproduce the computer models. We also provide the data in the figures as MATLAB figure files (Carreon, 2023c).

Acknowledgments
This research was funded by the Strategic University Research Partnership (SURP) program and through pre-Phase A mission concept funding for a Europa Lander, both of which were through the Jet Propulsion Laboratory, California Institute of Technology, under a contract with the National Aeronautics and Space Administration (SURP 80NM0018D0004). We give a special thanks to Tom Nordheim, Jeffrey Foster, Jake Kosberg, and Ben Furst for their experimental work and theoretical insight.

References

Amstutz, G. C. (1958). On the formation of snow penitentes. *Journal of Glaciology*, *3*(24), 304–311. https://doi.org/10.1017/s0022143000023972
Bergeron, V., Berger, C., & Betterton, M. (2006). Controlled irradiative formation of penitentes. *Physical Review Letters*, *96*(9), 098502. https://doi.org/10.1103/physrevlett.96.098502
Berisford, D., Foster, J., Kosberg, J., Furst, B., Poston, M., Daimaru, T., et al. (2021). Erosion of penitentes under experimental conditions relevant to ice-covered airless worlds. *Journal of Geophysical Research: Planets*, *126*(10), e2021JE006955. https://doi.org/10.1029/2021je006955
Berisford, D., Furst, B., Foster, J., Poston, M., Schoelen, D., Sahu, D., et al. (2018). Laboratory simulation of sublimating planetary surface ices: Experiment design and thermal considerations.
Betterton, M. (2001). Theory of structure formation in snowfields motivated by penitentes, suncups, and dirt cones. *Physical Review E*, *63*(5), 056129. https://doi.org/10.1103/physreve.63.056129
Briegleb, B., & Light, B. (2007). A delta-eddington multiple scattering parameterization for solar radiation in the sea ice component of the community climate system model. NCAR Technical Note NCAR/TN-472+ STR (pp. 1–108).
Carlson, R., Calvin, W., Dalton, J., Hansen, G., Hudson, R., Johnson, R., et al. (2009). Europa's surface composition. *Europa*, 283–328. https://doi.org/10.2307/j.ctt1xp3wdw.18
Carreon, A. (2023a). Figure 1.1 from carreon et. al. 2023. *figshare*. Retrieved from https://figshare.com/articles/figure/Figure_1_1_from_Carreon_et_al_2023/22198708/1
Carreon, A. (2023b). Led bar spectrum from carreon. et. al. 2023, figure a4. *figshare*. Retrieved from https://figshare.com/articles/dataset/LED_Bar_Spectrum_from_Carreon_et_al_2023_Figure_A4/22198948/1
Carreon, A. (2023c). Matlab figure files. *figshare*. Retrieved from https://figshare.com/articles/dataset/MATLAB_Figure_Files/23732223/1
Cathles, L. M., Abbot, D. S., Bassis, J. N., & MacAYEAL, D. R. (2011). Modeling surface-roughness/solar-ablation feedback: Application to small-scale surface channels and crevasses of the Greenland ice sheet. *Annals of Glaciology*, *52*(59), 99–108. https://doi.org/10.3189/172756411799096268
Chandrasekhar, S. (1960). *Radiative transfer*. Dover Publication.
Claudin, P., Jarry, H., Vignoles, G., Plapp, M., & Andreotti, B. (2015). Physical processes causing the formation of penitentes. *Physical Review E*, *92*(3), 033015. https://doi.org/10.1103/physreve.92.033015
Devroye, L. (1986). General principles in random variate generation. *Non-Uniform Random Variate Generation*, 27–82. https://doi.org/10.1007/978-1-4613-8643-8_2
Grenfell, T. C., & Warren, S. G. (1999). Representation of a nonspherical ice particle by a collection of independent spheres for scattering and absorption of radiation. *Journal of Geophysical Research*, *104*(D24), 31697–31709. https://doi.org/10.1029/1999jd900496
Grundy, W., & Schmitt, B. (1998). The temperature-dependent near-infrared absorption spectrum of hexagonal H_2O ice. *Journal of Geophysical Research*, *103*(E11), 25809–25822. https://doi.org/10.1029/98je00738
Hand, K., Berisford, D., Daimaru, T., Foster, J., Hofmann, A., & Furst, B. (2020). Penitente formation is unlikely on Europa. *Nature Geoscience*, *13*(1), 17–19. https://doi.org/10.1038/s41561-019-0496-2
He, C., & Flanner, M. (2020). Snow albedo and radiative transfer: Theory, modeling, and parameterization. In *Springer series in light scattering* (pp. 67–133). Springer.
Henyey, L. G., & Greenstein, J. L. (1941). Diffuse radiation in the galaxy. *The Astrophysical Journal*, *93*, 70–83. https://doi.org/10.1086/144246
Hobley, D. E., Moore, J. M., Howard, A. D., & Umurhan, O. M. (2018). Formation of metre-scale bladed roughness on Europa's surface by ablation of ice. *Nature Geoscience*, *11*(12), 901–904. https://doi.org/10.1038/s41561-018-0235-0
Jacques, S. L., & Wang, L. (1995). Monte Carlo modeling of light transport in tissues. In *Optical-thermal response of laser-irradiated tissue* (pp. 73–100). Springer.
Jia, X., Kivelson, M. G., Khurana, K. K., & Kurth, W. S. (2018). Evidence of a plume on Europa from Galileo magnetic and plasma wave signatures. *Nature Astronomy*, *2*(6), 459–464. https://doi.org/10.1038/s41550-018-0450-z
Kaempfer, T. U., Hopkins, M., & Perovich, D. (2007). A three-dimensional microstructure-based photon-tracking model of radiative transfer in snow. *Journal of Geophysical Research*, *112*(D24), D24113. https://doi.org/10.1029/2006jd008239
Kauzmann, W., & Eisenberg, D. (1969). *The structure and properties of water*. Clarendon Press.
Kokhanovsky, A. A., & Zege, E. P. (2004). Scattering optics of snow. *Applied Optics*, *43*(7), 1589–1602. https://doi.org/10.1364/ao.43.001589
Kopp, G., & Lean, J. L. (2011). A new, lower value of total solar irradiance: Evidence and climate significance. *Geophysical Research Letters*, *38*(1), L01706. https://doi.org/10.1029/2010gl045777
Lhermitte, S., Abermann, J., & Kinnard, C. (2014). Albedo over rough snow and ice surfaces. *The Cryosphere*, *8*(3), 1069–1086. https://doi.org/10.5194/tc-8-1069-2014
Lliboitry, L. (1954). The origin of penitents. *Journal of Glaciology*, *2*(15), 331–338. https://doi.org/10.1017/s0022143000025181
Macias, A., Carreon, A., Berisford, D. F., Nordheim, T. A., Kale, G., Goldstein, D., et al. (2023). Molecular transport conditions required for the formation of penitentes on airless, ice-covered worlds, with specific application to Europa, Enceladus, and Callisto. *Journal of Geophysical Research: Planets*, *128*(5), e2021JE007106. https://doi.org/10.1029/2021je007106
Matson, D. L., & Brown, R. H. (1989). Solid-state greenhouse and their implications for icy satellites. *Icarus*, *77*(1), 67–81. https://doi.org/10.1016/0019-1035(89)90007-9
Mätzler, C. (2002). MATLAB functions for Mie scattering and absorption, version 2.
Mie, G. (1908). Contributions to the optics of diffuse media, especially colloid metal solutions. *Annals of Physics*, *25*(3), 377–445. https://doi.org/10.1002/andp.19083300302
Molaro, J. L., Choukroun, M., Phillips, C. B., Phelps, E. S., Hodyss, R., Mitchell, K. L., et al. (2019). The microstructural evolution of water ice in the solar system through sintering. *Journal of Geophysical Research: Planets*, *124*(2), 243–277. https://doi.org/10.1029/2018je005773
Moores, J. E., Smith, C. L., Toigo, A. D., & Guzewich, S. D. (2017). Penitentes as the origin of the bladed terrain of Tartarus dorsa on Pluto. *Nature*, *541*(7636), 188–190. https://doi.org/10.1038/nature20779

Nguyen, T. G., Smith, C. L., Innanen, A., & Moores, J. E. (2019). Simulating the formation of Martian penitentes. *Planetary and Space Science*, *174*, 21–31. https://doi.org/10.1016/j.pss.2019.05.003

Owen, A. B. (2013). Monte Carlo theory, methods and examples.

Planck, M. (1914). *The theory of heat radiation*. Blakiston.

Prem, P., Goldstein, D., Varghese, P., & Trafton, L. (2019). Coupled DSMC-Monte Carlo radiative transfer modeling of gas dynamics in a transient impact-generated lunar atmosphere. *Icarus*, *326*, 88–104. https://doi.org/10.1016/j.icarus.2019.02.036

Rohatgi, A. (2022). Webplotdigitizer: Version 4.6. Retrieved from https://automeris.io/WebPlotDigitizer

Shampine, L. F., & Reichelt, M. W. (1997). The MATLAB ode suite. *SIAM Journal on Scientific Computing*, *18*(1), 1–22. https://doi.org/10.1137/s1064827594276424

Spencer, J. R., Tamppari, L. K., Martin, T. Z., & Travis, L. D. (1999). Temperatures on Europa from Galileo photopolarimeter-radiometer: Nighttime thermal anomalies. *Science*, *284*(5419), 1514–1516. https://doi.org/10.1126/science.284.5419.1514

Stamnes, K., Tsay, S.-C., Wiscombe, W., & Jayaweera, K. (1988). Numerically stable algorithm for discrete-ordinate-method radiative transfer in multiple scattering and emitting layered media. *Applied Optics*, *27*(12), 2502–2509. https://doi.org/10.1364/ao.27.002502

Sturm, M., Holmgren, J., König, M., & Morris, K. (1997). The thermal conductivity of seasonal snow. *Journal of Glaciology*, *43*(143), 26–41. https://doi.org/10.1017/s0022143000002781

Tanikawa, T., Aoki, T., Hori, M., Hachikubo, A., Abe, O., & Aniya, M. (2006). Monte Carlo simulations of spectral albedo for artificial snowpacks composed of spherical and nonspherical particles. *Applied Optics*, *45*(21), 5310–5319. https://doi.org/10.1364/ao.45.005310

Tiedje, T., Mitchell, K. A., Lau, B., Ballestad, A., & Nodwell, E. (2006). Radiation transport model for ablation hollows on snowfields. *Journal of Geophysical Research*, *111*(F2), F02015. https://doi.org/10.1029/2005jf000395

Titus, T., & Cushing, G. (2012). Thermal diffusivity experiment at the grand falls dune field. In *Third international planetary dunes workshop: Remote sensing and data analysis of planetary dunes* (Vol. 1673, pp. 95–96).

Troll, C. (1942). Büsserschnee in den hochgebirgen der erde: ein beitrag zur geographie der schneedecke und ihrer ablationsformen. *Perthes*.

Van de Hulst, H. C. (2012). *Multiple light scattering: Tables, formulas, and applications*. Elsevier.

Warren, S. G. (1982). Optical properties of snow. *Reviews of Geophysics*, *20*(1), 67–89. https://doi.org/10.1029/rg020i001p00067

Warren, S. G., & Brandt, R. E. (2008). Optical constants of ice from the ultraviolet to the microwave: A revised compilation. *Journal of Geophysical Research*, *113*(D14), D14220. https://doi.org/10.1029/2007jd009744

Wiscombe, W. J., & Warren, S. G. (1980). A model for the spectral albedo of snow. I: Pure snow. *Journal of the Atmospheric Sciences*, *37*(12), 2712–2733. https://doi.org/10.1175/1520-0469(1980)037<2712:amftsa>2.0.co;2